Publications of the Astronomical Society of the Pacific, 138:104402 (23pp), 2026 October https://doi.org/10.1088/1538-3873/aeaf18
© 2026. The Author(s). Published by IOP Publishing Ltd on behalf of the Astronomical Society of the Pacific (ASP).

OPEN ACCESS

COSMOS-3D: Spectro-photometric Confirmation of Shabgard, A Cool, Metal-poor Brown Dwarf in the COSMOS Field

Bahareh S. Salmasi[1,2,3], Priyanka Jalan[1,4], Tomotsugu Goto[1,5], Tetsuya Hashimoto[6], Feige Wang[7], Tayyaba Zafar[2,3], Koki Kakiichi[8], Ece Kilerci[9], Srivardini Ayyappan[1,2,3], Romain A. Meyer[10], Anilkumar Mailvaganam[2,3], Tamal Mukherjee[2,3], Xuanyi Lyu[2], Imam Uzma Aalia[2,3], Arihant Raidani[2,3], Samuel Carlson[2,3], Jose Luis Carrillo Martinez[2,3], Andreas L. Faisst[11], Marko Shuntov[8,12], Hollis B. Akins[13], and Zihao Li[8]

COSMOS-3D Collaboration

[1] Institute of Astronomy, National Tsing Hua University, Hsinchu, Taiwan; physics.bahare@gmail.com
[2] School of Mathematical and Physical Sciences, Macquarie University, Sydney, NSW 2109, Australia
[3] Astrophysics and Space Technologies Research Centre, Macquarie University, Sydney, NSW 2109, Australia
[4] Center for Theoretical Physics, Polish Academy of Sciences, Al. Lotników 32/46, 02-668, Warsaw, Poland
[5] Department of Physics, National Tsing Hua University, Hsinchu, Taiwan
[6] Institute of Astronomy, National Chung Hsing University, Taichung, Taiwan
[7] Department of Astronomy, University of Michigan, Ann Arbor, MI, USA
[8] Cosmic Dawn Center (DAWN), Niels Bohr Institute, University of Copenhagen, Jagtvej 128, DK-2200 Copenhagen N, Denmark
[9] Department of Astronomy and Space Sciences, Science Faculty, İstanbul University, Beyazıt 34119, İstanbul, Türkiye
[10] Department of Astronomy, University of Geneva, Chemin Pegasi 51, 1290 Versoix, Switzerland
[11] IPAC, California Institute of Technology, 1200 E. California Blvd. Pasadena, CA 91125, USA
[12] University of Geneva, 24 rue du Général-Dufour, 1211 Genève 4, Switzerland
[13] Department of Astronomy, The University of Texas at Austin, 2515 Speedway Blvd Stop C1400, Austin, TX 78712, USA
Received 2026 August 14; revised 2026 September 18; accepted 2026 October 1; published 2026 October 26

Abstract

Brown dwarfs are unique laboratories for studying the physics of cool atmospheres, the low-mass end of star formation, and the transition between stars and giant planets. Their spectra encode the effects of temperature, gravity, metallicity, clouds, and disequilibrium chemistry, but identifying and characterizing the coldest brown dwarfs remains challenging, particularly at faint magnitudes in deep extragalactic surveys. We aim to establish the nature and atmospheric properties of COSMOS2025 ID 639188, hereafter Shabgard, a compact source previously selected as a brown-dwarf candidate from COSMOS-Web photometry on the basis of its point-source morphology and T/Y-dwarf-like NIRCam colors. In this work, we characterize this source using serendipitous JWST/NIRCam F444W wide-field slitless spectroscopy from COSMOS-3D. We extract its local-background-subtracted, profile-weighted 4.05–4.85 μm spectrum, combine it with COSMOS2025 NIRCam photometry, compare the data with six atmosphere-model families, and measure its motion using multi-epoch NIRCam imaging. The LOWZ atmosphere-grid fit, based on principal component analysis (PCA) interpolation and Markov Chain Monte Carlo (MCMC) sampling, gives $T_{\rm eff} = 718.6^{+10.6}_{-10.2}$ K and $[{\rm M/H}] = -1.00^{+0.07}_{-0.08}$, favoring a cool, subsolar-metallicity atmosphere characteristic of the late-T/Y transition. A fixed-atmosphere molecular-opacity test strongly favors a contribution from CH_4 to the observed 4–5 μm spectral shape. The restricted wavelength coverage, however, prevents a molecule-by-molecule abundance determination. Model-dependent physical estimates span approximately 23–52 $M_{\rm Jup}$ and 140–180 pc. We measure a proper motion of $|\mu| = 89.2 \pm 0.4$ mas yr^{-1}, while the LOWZ MCMC flux scaling gives a distance of $176.2^{+18.4}_{-17.8}$ pc, supporting the interpretation of Shabgard as a Galactic brown dwarf. Together, these results support its classification as a cool, metal-poor brown dwarf and demonstrate the ability of JWST deep-field surveys to discover and characterize faint Galactic substellar objects.

Unified Astronomy Thesaurus concepts: Brown dwarfs (185); T dwarfs (1679); Y dwarfs (1827); Spectroscopy (1558); Space telescopes (1547)

1. Introduction

Brown dwarfs are intermediate mass objects, between massive planets and the smallest hydrogen-burning stars. Their masses are generally described in terms of the deuterium

Original content from this work may be used under the terms of the Creative Commons Attribution 4.0 licence. Any further distribution of this work must maintain attribution to the author(s) and the title of the work, journal citation and DOI.

burning limit at $\sim 13 M_{\rm Jup}$ and the hydrogen burning limit at ~ 75–$80 M_{\rm Jup}$ (Burrows et al. 2001). However, both limitations rely on composition, helium percentage, and evolutionary history (Chabrier & Baraffe 2000; Spiegel et al. 2011). Because brown dwarfs do not sustain stable core hydrogen fusion, they cool and fade continuously with time. Their spectra therefore trace a sequence of decreasing effective temperature through late-M, L, T, and Y types, with strong sensitivity to condensate clouds, collision-induced H_2 absorption, H_2O, CH_4, CO, CO_2, NH_3, PH_3, and other molecular species (Burrows et al. 2001; Kirkpatrick 2005; Phillips et al. 2020; Marley et al. 2021; Mukherjee et al. 2024).

Brown dwarfs are important for both stellar and planetary astrophysics. They probe the low-mass end of star formation and the Galactic mass function (Luhman 2012; Kirkpatrick et al. 2021), and their atmospheres provide directly observable analogs of self-luminous giant exoplanets (Marley & Robinson 2015; Bowler 2016; Faherty et al. 2016). Their spectra respond to $T_{\rm eff}$, gravity, metallicity, clouds, and disequilibrium chemistry, so well-characterized brown dwarfs are essential benchmarks for atmospheric models used across the sub-stellar regime (Karalidi et al. 2021; Marley et al. 2021; Mukherjee et al. 2024). Old, metal-poor ultracool dwarfs are especially valuable because they can be used to study atmospheric physics in thick-disk and halo chemical environments where changes in opacity and collision-induced absorption alter colors and spectral shape (Jurić et al. 2008; Zhang et al. 2019; Meisner et al. 2021; A. J. Burgasser et al. 2024).

In deep extragalactic surveys, they are also a practical source-classification issue: cool Galactic dwarfs can be compact and red enough to contaminate high-redshift galaxy and active-galactic-nucleus samples (A. J. Burgasser et al. 2024; Hainline et al. 2024; Chen et al. 2025; Tu et al. 2025). The James Webb Space Telescope (JWST; Gardner et al. 2023) has substantially expanded the accessible volume for ultracool dwarf searches (Wang et al. 2023; Hainline et al. 2024). Its near-infrared sensitivity, together with low-resolution spectroscopy from NIRSpec/PRISM, covers the wavelength range where late-T and Y dwarfs show strong molecular absorption and continuum-shape diagnostics (Jakobsen et al. 2022; Rieke et al. 2023; Rigby et al. 2023). NIRSpec/PRISM observations have already confirmed cold brown dwarfs at kiloparsec-scale distances in deep extragalactic fields, including objects identified in the Ultradeep NIRSpec and NIRCam Observations before the Epoch of Reionization (UNCOVER; R. Bezanson et al. 2024) Treasury program and the Red Unknowns: Bright Infrared Extragalactic Survey (RUBIES; A. J. Burgasser et al. 2024). These detections show that JWST can extend spectroscopic studies of ultracool dwarfs to much larger distances than were previously accessible. However, interpreting such faint spectra remains challenging because the near-infrared continuum shape and broad molecular absorption features depend simultaneously on $T_{\rm eff}$, metallicity, surface gravity, cloud opacity, and vertical mixing (A. J. Burgasser et al. 2024; Mukherjee et al. 2024; Tu et al. 2025; Morrissey et al. 2026). Breaking these degeneracies typically requires both spectroscopy and external flux constraints, especially when only a limited wavelength range is available.

The COSMOS field provides a useful setting for our search because it combines deep multi-wavelength imaging with new wide-area JWST observations. In particular, COSMOS-Web supplies the photometric data for identifying compact red brown-dwarf candidates, while COSMOS-3D adds NIRCam/F444W wide-field slitless spectroscopy (Casey et al. 2023; Shuntov et al. 2025; Meyer et al. 2026). Although the F444W grism window is narrower than a full NIRSpec/PRISM spectrum, it covers the 4–5μm region where cool T/Y-like atmospheres are shaped by molecular opacity from species such as H_2O, CH_4, CO, and CO_2 (A. J. Burgasser et al. 2024; Mukherjee et al. 2024). It therefore provides a useful spectroscopic test of photometrically selected ultracool-dwarf candidates when combined with broadband JWST photometry.

In this work, we use COSMOS-Web photometry and COSMOS-3D NIRCam/F444W WFSS spectroscopy to test a photometrically selected brown-dwarf candidate in the COSMOS field. We start from the COSMOS-Web brown-dwarf candidate catalog of (Festin et al. 2026), and inspect the available COSMOS-3D Unfold products, including both the two-dimensional grism coadds and the associated one-dimensional spectra. Among the candidates with available spectroscopy, COSMOS2025[14] ID 639188 was selected for detailed analysis because its F444W trace is centered and relatively isolated, and its local background optimal extraction yields a flux scale consistent with the COSMOS2025 photometry. For readability, we hereafter refer to this source as Shabgard, from the Persian word shabgard (night wanderer), while retaining COSMOS2025 ID 639188 as its formal catalog identifier.

To our knowledge, this is the first spectrophotometric analysis of this source. We extract and validate its F444W WFSS spectrum, combine it with broadband JWST/NIRCam photometry, and compare the data with several brown-dwarf atmosphere and evolutionary model families. We aim to investigate which properties can be constrained by the present data, particularly $T_{\rm eff}$, surface gravity, metallicity, distance, and mass, and which remain uncertain because of the restricted F444W wavelength coverage.

This paper is organized as follows. In Section 2, we describe the photometric candidate selection, the COSMOS2025 catalog measurements, and the COSMOS-3D WFSS data. Section 3 presents the local-background optimal extraction of the F444W spectrum. Section 4 describes the atmosphere-model comparison, synthetic photometry, weighting scheme, LOWZ atmosphere-model interpolation, MCMC analysis, and the molecular-opacity and empirical spectral tests. Section 5

[14] https://cosmos2025.iap.fr/catalog.html

presents the atmosphere-model results, inferred physical parameters, multi-epoch proper-motion measurement, and supplementary machine learning consistency test. In Section 6, we discuss the brown-dwarf interpretation, Galactic kinematics, agreement and differences among the model families, and limitations of the current data. We summarize our conclusions in Section 7.

2. Candidate Selection and Data

This section describes how Shabgard (COSMOS2025 ID 639188) was selected and which observational data are used in the analysis. We first summarize the photometric brown-dwarf candidate selection from the COSMOS2025 catalog, then describe the COSMOS-Web photometry and COSMOS-3D NIRCam/F444W WFSS products used for the spectrophotometric analysis. We also explain why Shabgard was chosen for detailed follow-up from the subset of candidates with available grism spectra.

2.1. COSMOS-Web Photometry and COSMOS-3D WFSS Spectroscopy

This work is based on the combination of COSMOS-Web imaging, COSMOS2025 catalog photometry, and COSMOS-3D slitless spectroscopy. The Cosmic Evolution Survey (COSMOS) field is a $\sim$2 deg^2 equatorial field with extensive multi-wavelength imaging and spectroscopy from X-ray to radio wavelengths (Scoville et al. 2007). This makes it a particularly useful field for identifying rare compact sources and for checking their photometric and morphological properties across many bands.

COSMOS-Web, the JWST Cosmic Origins Survey, is a Cycle 1 Treasury program covering the central COSMOS region with wide-area JWST imaging (Casey et al. 2023). The survey provides NIRCam imaging in F115W, F150W, F277W, and F444W over $\sim$0.54 deg^2, together with MIRI/F770W imaging over a smaller $\sim$0.19 deg^2 area (Casey et al. 2023; Franco et al. 2026). For the broadband photometric constraints in this paper, we use the COSMOS2025 master catalog (Shuntov et al. 2025). In this paper, the COSMOS2025 photometry is used as the broadband SED constraint, with the F444W point providing the main flux anchor for comparison with the grism spectrum.

The spectroscopic data come from COSMOS-3D, which adds JWST/NIRCam wide-field slitless spectroscopy (WFSS) in F444W across $\sim$0.33 deg^2 within the COSMOS-Web region [K. Kakiichi et al. 2026, (in preparation)]. The spectroscopic data used in this work are the COSMOS-3D NIRCam/F444W WFSS products generated with the `unfold_jwst` reduction framework (Wang et al. 2023; Yang et al. 2023; F. Wang et al. 2026). The available products include two-dimensional spectral coadds containing the science, inverse-variance, mask, wavelength, and model-trace information, together with associated one-dimensional coadd spectra. Since the source is contaminated by nearby bright star spikes, we use the two-dimensional Unfold product as the input to the local-background, profile-weighted re-extraction described in Section 3. The COSMOS-3D observing program and survey design are described by [K. Kakiichi et al. 2026 (in preparation)].

The NIRCam long-wavelength grisms provide slitless spectra with resolving power $R \sim 1600$ near 4μm (Greene et al. 2017). In the F444W configuration, the first-order spectra cover approximately 3.9–5.0 μm.[15] This wavelength range provides the spectroscopic basis for the COSMOS-3D analysis used in this paper.

2.2. Photometric Pre-selection

The target studied in this paper, Shabgard (COSMOS2025 ID 639188), is drawn from the COSMOS-Web photometric brown-dwarf candidate catalog of (Festin et al. 2026). That catalog starts from the COSMOS2025 v1.0 source list, which contains approximately 8×10^5 sources over the full 0.54 deg^2 COSMOS-Web area, and applies a staged selection designed to isolate compact sources with T/Y-dwarf-like SEDs. In brief, the (Festin et al. 2026) selection uses: (1) an F444W signal-to-noise requirement, with F444W emphasized because the $\sim$4.5μm window is often the highest-S/N JWST/NIRCam band for cool T/Y dwarfs; (2) catalog quality cuts, including `warn_flag=0` and rejection of strongly blended or stellar-contamination-flagged sources; (3) COSMOS2025 point-source morphology/type information; (4) color cuts targeting the blue short-wavelength and red F277W–F444W behavior expected for cool brown dwarfs; and (5) visual inspection of JWST cutouts and public COSMOS-Web SED panels. The filtering sequence reduces the parent catalog from $\sim 8 \times 10^5$ sources to 76 brown-dwarf candidates, including Shabgard (ID 639188) (Festin et al. 2026).

We next inspected the available COSMOS-3D Unfold products for the 76 photometric brown-dwarf candidates from (Festin et al. 2026). In the current reduction, 36 of these candidates have associated COSMOS-3D spectral files. Most of these spectra are not suitable for direct atmospheric fitting, either because the continuum signal is too weak, the trace is affected by overlapping slitless spectra, the source lies close to a wavelength edge, or the local background is difficult to define in crowded regions. After inspecting both the two-dimensional coadds and the default one-dimensional spectra, we identified six candidates with centered and sufficiently isolated F444W traces for possible continuum extraction. The extraction diagnostics for these six sources are presented in Appendix A.1. ID 639188 is the brightest F444W source among the 76 candidates in the parent sample and, among the

[15] See the JWST User Documentation for NIRCam grisms: https://jwst-docs.stsci.edu/jwst-near-infrared-camera/nircam-instrumentation/nircam-grisms.

Table 1
COSMOS2025 Photometry for Shabgard

Band	AB mag	AB mag error	f_ν [μJy]	σ_{f_ν} [μJy]
F115W	24.196	0.011	0.7615	0.0075
F150W	24.851	0.011	0.4167	0.0042
F277W	25.615	0.019	0.2061	0.0037
F444W	22.215	0.003	4.7216	0.0119

Note. Flux densities and uncertainties are taken from the COSMOS2025 catalog columns. Model fitting uses these values with the additional error floors described in Section 4.

six candidates with suitable traces, it also gives the most stable extraction and the clearest agreement between the extracted F444W flux scale and the COSMOS2025 photometry. We therefore select it, before any atmosphere-model fitting, as the best-characterized candidate for this case-study analysis, and adopt Shabgard for the detailed spectrophotometric analysis in this paper.

For Shabgard, we adopt the COSMOS2025 position of ID 639188, R.A. $=150.^{\circ}0634341$ and Decl. $=+2.^{\circ}3552216$. The source has `warn_flag`=0 and appears compact in the JWST/NIRCam imaging. In the independent photometric selection of (Festin et al. 2026), the object is also favored by the stellar-template solution over the galaxy-template solution, with $\chi^2_{\rm star} = 33.58$ and $\chi^2_{\rm galaxy} = 147317$ in their LePhare configuration (Arnouts et al. 1999; Ilbert et al. 2006). Both fits use the same photometry, degrees of freedom, and extinction assumptions, allowing a direct comparison of the two χ^2 values and strongly disfavoring a normal galaxy SED. The photometry used in the model fitting is summarized in Table 1. Shabgard is red from F277W to F444W, with F277W-F444W$\simeq$3.40 mag in the current catalog columns.

3. Local-background Profile-weighted Extraction

For our analysis, we perform a custom one-dimensional re-extraction of Shabgard from the COSMOS-3D `unfold_jwst` two-dimensional `coadd2d` product, rather than adopting the supplied `coadd1d` spectrum directly. The upstream Unfold products provide the calibrated two-dimensional science image, inverse-variance map, pixel mask, wavelength solution, and model-trace information (Wang et al. 2023). Our subsequent processing is limited to the local-background estimation, profile-weighted extraction, masking, and quality checks described below.

This additional extraction step is motivated by the nature of slitless spectroscopy, in which all sources in the field are dispersed and faint continuum spectra can be affected by overlapping spectral wings, residual structure from neighboring traces, and a spatially varying background. Similar challenges are commonly addressed through source-dependent trace definitions, contamination modeling, and extraction apertures tied to the direct-image morphology or spectral trace (Kümmel et al. 2009; Brammer et al. 2012; Momcheva et al. 2016).

The extraction geometry for Shabgard is shown in Figure 1. The initial trace center is determined automatically from the peak of the wavelength-collapsed `MODEL` spatial profile, and the trace is then followed as a function of wavelength within a ± 7 pixel search window and median-smoothed along the dispersion direction. We adopt a source half-width of 5 spatial pixels. On each side of the wavelength-dependent trace center, candidate background pixels are selected between offsets of 6 and 16 spatial pixels. Thus, the inner background boundary is located approximately one pixel beyond the nominal source-aperture boundary; the value of 6 pixels is measured from the trace center rather than from the edge of the source aperture. Depending on the subpixel trace position, zero or one unused detector row lies between the source and background selections. These values were chosen after testing reasonable alternatives and were found to produce stable fluxes.

We tested the sensitivity of the extraction to nearby reasonable geometries by varying the source half-width from 4 to 6 pixels, the inner background offset from 5 to 7 pixels, and the background width from 8 to 12 pixels. Across the resulting 27 extractions, the synthetic F444W flux has a median of 4.94 μJy and a central 68% range of 4.78–5.09 μJy. The adopted configuration gives 4.94 μJy, indicating that the extracted flux is not strongly sensitive to the exact aperture and background geometry.

Before extraction, we construct a valid-pixel mask requiring finite science values, finite positive inverse variance, and a positive `MASK` value. We also apply a conservative two-dimensional bad-pixel rejection along each spatial row, using a local running median and rejecting only isolated 8σ outliers. This step is intended to remove hot pixels or narrow detector artifacts without suppressing broad spectral structure.

The local background is estimated independently in each wavelength column. Background pixels are first sigma-clipped using the median and a median-absolute-deviation estimate of the scatter. If valid background pixels are available on both sides of the trace, we fit a weighted linear function of spatial row and evaluate this model across the source aperture. If only one side of the background region is usable, or if the linear fit is unstable, we instead subtract a constant background equal to the sigma-clipped median of the remaining valid background pixels in that column. This provides a local column-by-column background subtraction before the one-dimensional extraction.

The final one-dimensional spectrum is extracted using a profile-weighted estimator following (Horne 1986). For each wavelength column, the spatial profile P_{ij} is taken from the non-negative `MODEL` image and normalized over the valid source pixels. If the model profile is unavailable or pathologically narrow, we use a Gaussian fallback profile

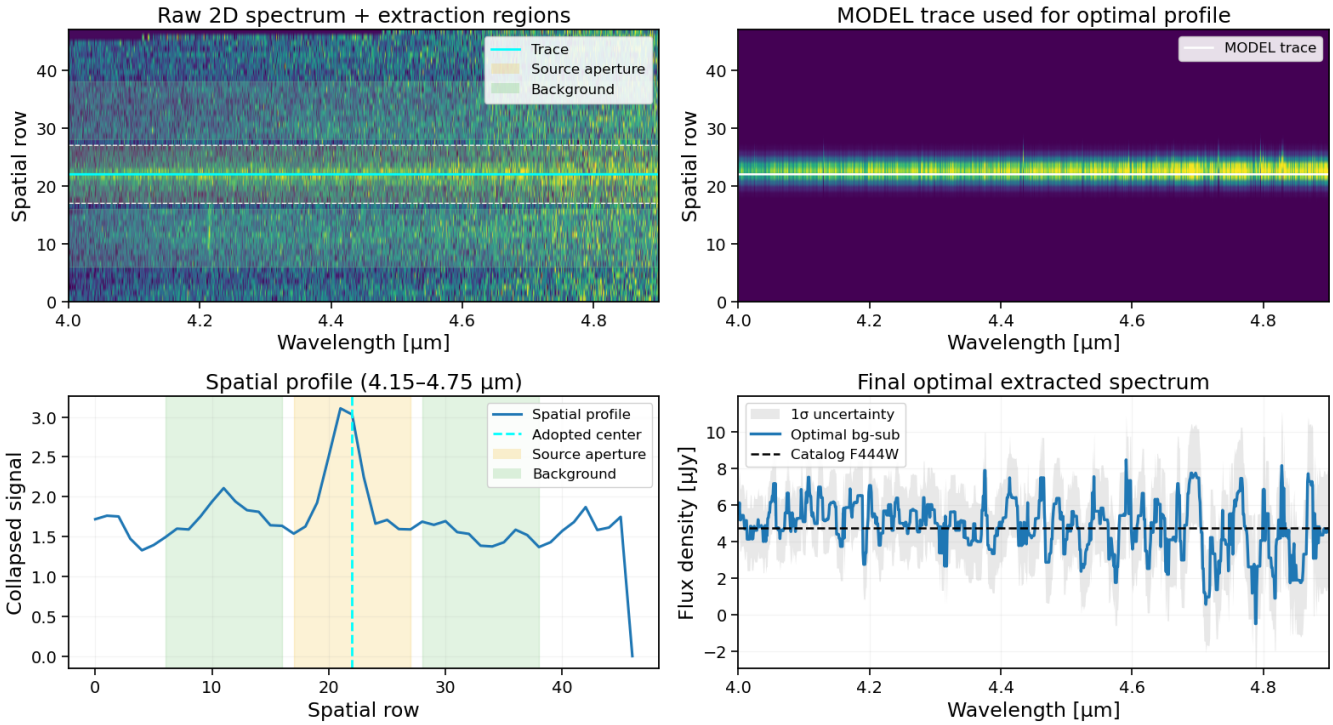


Figure 1. Local-background optimal extraction for Shabgard. The upper-left panel shows the two-dimensional F444W WFSS spectrum with the traced source position, source aperture, and local background regions. The upper-right panel shows the corresponding `MODEL` trace used to define the optimal-extraction profile. The lower-left panel shows the spatial profile collapsed over the central wavelength range, with the adopted source and background regions marked. The lower-right panel shows the final local-background-subtracted optimal one-dimensional spectrum, with the COSMOS2025 F444W catalog flux shown for comparison.

centered on the trace with $\sigma = 1.4$ spatial pixels. The extracted flux density in column j is then computed as

$$f_j = \frac{\sum_i P_{ij}[D_{ij} - B_{ij}]w_{ij}}{\sum_i P_{ij}^2 w_{ij}}, \quad (1)$$

where D_{ij} is the two-dimensional science image, B_{ij} is the fitted local background evaluated over the source aperture, and w_{ij} is the inverse-variance weight after masking. The corresponding formal variance is

$$\sigma_{f,j}^2 = \frac{1}{\sum_i P_{ij}^2 w_{ij}}. \quad (2)$$

This formal variance assumes independent pixels and does not account for covariance introduced by resampling of the `coadd2d` data. For the final fitting vector, we keep only columns with finite wavelength, flux, and uncertainty, at least two valid source pixels, at least four valid background pixels, and wavelengths in the range 4.05–4.85 μm. For Shabgard, this gives 816 usable wavelength pixels out of 1302 columns in the `coadd2d` spectrum.

As a flux-scale validation, we compare synthetic F444W photometry measured from the extracted spectra with the COSMOS2025 catalog value. The synthetic photometry is computed with the F444W throughput curve using the photon-weighted mean flux density.

The local-background profile-weighted extraction gives synthetic F444W fluxes of 4.858 μJy over the full usable wavelength range and 4.950 μJy over the trimmed fitting range, in good agreement with the COSMOS2025 catalog value of 4.7216 μJy. As an independent check, a simple local-background aperture extraction gives similar values of 4.950 μJy and 4.898 μJy over the same two wavelength ranges. In contrast, the default pipeline one-dimensional spectrum gives substantially larger synthetic F444W fluxes of 16.31 μJy and 13.48 μJy. We therefore adopt the local-background profile-weighted spectrum for the atmosphere-model fitting and use the pipeline spectrum only as an extraction diagnostic.

The same extraction diagnostics for the other centered-trace candidates are shown in Appendix Figure A1.

4. Atmosphere-model Fitting Methods

The atmosphere-model comparison is designed as a cross-model consistency test rather than as a formal retrieval from a single atmosphere grid. Because the available spectrum covers only the NIRCam/F444W grism window, different combinations of temperature, gravity, metallicity, vertical mixing, and

Table 2
Brown-dwarf Atmosphere Model Families used in the Final Comparison

Compact Name	Full Name and Reference	Main Model Physics/Parameters	Role in this Paper
Sonora Elf Owl	Sonora Substellar Atmosphere Models IV: Elf Owl (Mukherjee et al. 2024)	Cloud-free, self-consistent atmospheres including disequilibrium chemistry, metallicity, C/O ratio, and vertical mixing parameterized by K_{zz}.	Tests chemical degeneracies in the 3-5 μm region, especially among metallicity, C/O, and vertical mixing.
LOWZ	Low-metallicity ultracool-dwarf atmosphere grid distributed through `ucdmcmc` (Meisner et al. 2021; Lueber & Burgasser 2025)	Low-temperature and low-metallicity atmosphere models motivated by T-subdwarf studies. The fitted parameters include $T_{\rm eff}$, $\log g$, [M/H], and a dilution factor.	Primary low-metallicity test and the model family used for the PCA-interpolated MCMC analysis.
SAND	Spectral ANalog of Dwarfs model family (Alvarado et al. 2024; Lueber & Burgasser 2025)	Ultracool-dwarf atmosphere grid with leverage on metallicity and abundance patterns, including $T_{\rm eff}$, $\log g$, [M/H], and [α/Fe].	Independent test of a cool, metal-poor brown-dwarf interpretation.
Sonora Bobcat	The Sonora Brown Dwarf Atmosphere and Evolution Models. I: cloudless atmospheres in rainout chemical equilibrium (Marley et al. 2021)	Cloud-free atmosphere and evolutionary models with rainout chemistry, spanning substellar temperatures, gravities, metallicities, radii, masses, and ages.	Independent cloud-free atmosphere/evolution check on the preferred temperature and physical scale.
Morley cloudy models	Cloudy T/Y-dwarf atmosphere models including sulfide and salt condensate clouds (Morley et al. 2012)	Cool brown-dwarf atmospheres with condensate-cloud opacity, commonly parameterized by the sedimentation efficiency $f_{\rm sed}$.	Tests whether possible cloud opacity can also reproduce the observed SED and F444W continuum shape. This is used as a cloud-systematics check, not as a direct cloud detection.
ATMO2020/++	ATMO cool brown-dwarf and giant-exoplanet atmosphere/evolution models (Phillips et al. 2020; Leggett et al. 2021; Meisner et al. 2023)	Cool T/Y atmosphere and evolutionary models with an independent treatment of temperature-pressure structure, chemistry, and substellar evolution.	Independent model-family check on the preferred temperature, gravity, and evolutionary interpretation.

cloud opacity can produce similar broad-band behavior. We therefore compare Shabgard with six brown-dwarf atmosphere model families and focus on the physical conclusions that remain stable across different model assumptions.

4.1. Model Families

The final model comparison includes six atmosphere model families: Sonora Elf Owl, LOWZ, SAND, Sonora Bobcat, Morley cloudy models, and ATMO2020/ATMO2020++. These grids were chosen because they test complementary aspects of cool brown-dwarf atmospheres, including metallicity, surface gravity, C/O ratio, vertical mixing, cloud-free chemistry, evolutionary consistency, and possible condensate-cloud opacity. Table 2 gives the compact names, full model names, main physical content, and role of each model family in this paper.

The use of multiple grids is important because each family encodes different assumptions about atmospheric chemistry and opacity. Sonora Elf Owl and Sonora Bobcat provide cloud-free comparisons, but with different chemical assumptions and parameter coverage. LOWZ and SAND are especially useful for testing subsolar-metallicity solutions. The Morley cloudy grid is included because cool T/Y-dwarf atmospheres can be affected by sulfide and salt condensate clouds; therefore, we also test whether cloud opacity could plausibly contribute to the observed spectral shape. Because the current data cover only the F444W grism interval, we do not interpret the cloud-model comparison as evidence for a detected cloud feature. Instead, it is used to estimate how strongly the atmospheric interpretation depends on the choice of cloud-free versus cloudy models.

4.2. Synthetic Photometry, Weighting, and Fit Metrics

All model spectra are converted to the same observational space before fitting. Each model is placed on an F_ν flux-density scale, smoothed to the approximate NIRCam/WFSS resolution, interpolated onto the observed wavelength grid, and integrated through the JWST/NIRCam filter curves to produce synthetic photometry. For both the observed spectrum and the models, synthetic band fluxes are computed using the photon-weighted mean flux density,

$$\langle f_\nu \rangle = \frac{\int f_\nu(\lambda)\, T(\lambda)\, \lambda^{-1}\, d\lambda}{\int T(\lambda)\, \lambda^{-1}\, d\lambda}, \tag{3}$$

where $T(\lambda)$ is the total system throughput of the filter. This convention is used consistently for the COSMOS2025 photometry comparison and for synthetic F444W fluxes measured from the extracted WFSS spectrum.

For each model, we solve for a positive multiplicative scale factor between the model and the data. For observed fluxes f_i, model fluxes m_i, uncertainties σ_i, and optional relative weights

w_i, the weighted least-squares normalization is

$$a = \frac{\sum_i w_i f_i m_i/\sigma_i^2}{\sum_i w_i m_i^2/\sigma_i^2}. \quad (4)$$

For most model-family comparisons, this scale is treated only as the best normalization needed to compare model shape and photometry. For surface-flux model grids, however, the normalization can have a physical interpretation. In the LOWZ MCMC analysis, we therefore fit the dilution factor $\alpha = (R/d)^2$, where R is the object radius and d is the distance.

The likelihood uses the local-background, profile-weighted WFSS spectrum over 4.05–4.85 μm together with the available JWST/NIRCam photometry. We adopt empirical error floors of 8% plus 0.05 μJy for the spectral points and 5% for the photometric points. The spectral floor is conservative compared with the scatter among the alternative extraction geometries described above. We also repeated the model comparison using photometric floors of 3%, 5%, and 10%. The preferred parameters remain unchanged across this range. These floors are intentionally conservative because the dominant uncertainty is not purely photon noise: background subtraction, trace placement, residual slitless contamination, and model imperfections can all contribute additional systematic residuals.

The F444W photometric point is given the largest relative weight in the photometric part of the fit because it anchors the absolute flux scale over the same wavelength region sampled by the WFSS spectrum. This prevents the noisy grism continuum from moving the model normalization away from the COSMOS2025 broad-band flux, while still allowing the F444W spectral shape to constrain the atmosphere. The remaining NIRCam bands provide the broader SED context.

For reporting and ranking the grid-search fits, we compute separate mean spectroscopic and weighted-mean photometric squared-residual diagnostics. The spectroscopic contribution is defined as

$$\overline{\chi^2}_{\rm spec} = \frac{1}{N_{\rm spec}} \sum_{j=1}^{N_{\rm spec}} \left[\frac{f_j - a m_j}{\sigma_j} \right]^2, \quad (5)$$

where f_j and m_j are the observed and model spectral flux densities, σ_j is the corresponding uncertainty, and a is the fitted multiplicative normalization.

The photometric contribution is the weighted mean

$$\overline{\chi^2}_{{\rm phot},w} = \frac{\sum_b w_b \left[\frac{F_b - a M_b}{\sigma_b} \right]^2}{\sum_b w_b}, \quad (6)$$

where F_b and M_b are the observed and synthetic model flux densities in band b, and w_b is the adopted relative band weight. We use $w_b = 1$ for F115W, F150W, and F277W and $w_b = 10$ for F444W, so that F444W provides the strongest photometric constraint over the wavelength region sampled directly by the WFSS spectrum.

The balanced ranking objective is

$$Q_{\rm bal} = \overline{\chi^2}_{\rm spec} + 2\,\overline{\chi^2}_{{\rm phot},w}. \quad (7)$$

Because the F444W photometric constraint overlaps the WFSS wavelength range, and because the relative weights and error floors are empirical, $Q_{\rm bal}$ is a weighted pseudo-χ^2 objective used only to rank models consistently. It is not interpreted using a formal χ^2 probability distribution.

The multiplicative normalization a is solved by minimizing this same objective, so the adopted spectral, photometric, and band weights are applied consistently in both the normalization and the model ranking. The resulting $Q_{\rm bal}$ values are used for relative comparison of the discrete atmosphere-grid solutions; quantitative parameter uncertainties for LOWZ are derived separately from the likelihood-based MCMC analysis. The fitted vector contains 816 spectral points and four photometric points. For each fixed grid model, one multiplicative normalization is fitted, corresponding nominally to 819 residual degrees of freedom. However, spectral resampling covariance and the overlapping F444W constraints prevent these from being interpreted as independent formal degrees of freedom.

In addition to χ^2, we compute the cosine similarity of the WFSS spectral shape,

$$\cos\theta = \frac{\sum_j f_j m_j}{\left(\sum_j f_j^2\right)^{1/2} \left(\sum_j m_j^2\right)^{1/2}}. \quad (8)$$

Cosine similarity is a standard vector-space similarity measure originally developed in information retrieval and pattern matching (Salton et al. 1975). Here it is used only as a secondary diagnostic of spectral-shape agreement. The model ranking and physical interpretation are not based on cosine similarity alone.

4.3. LOWZ PCA-interpolated MCMC

The LOWZ atmosphere grid is discrete, so we constructed a continuous interpolator before sampling. We fixed C/O=0.55 and $\log K_{zz} = -1.0$ to the values of the preferred discrete LOWZ solution and interpolated over $T_{\rm eff}$, $\log g$, and [M/H]. After fixing these chemistry parameters, the grid contains 17 values of $T_{\rm eff}$ spanning 500-–1600 K, five values of $\log g$ spanning 3.5–5.25, and 11 values of [M/H] spanning −2.5 to +1.0. Of the 935 possible grid nodes, 931 are available, corresponding to 99.6% completeness. The four missing nodes were filled by local interpolation from the surrounding available models before constructing the regular interpolator.

At each grid node, we formed the same 820-element model vector used in the likelihood, containing the 816 F444W spectral elements and the four NIRCam photometric fluxes. The spectral and photometric components were scaled to reproduce the relative weighting defined in Section 4.2. Before applying principal-component analysis (PCA; Jolliffe & Cadima 2016), each element was divided by its corresponding uncertainty and the model vectors were mean-centered. We retained the minimum number of principal components required to explain 99.99% of the weighted model variance. Six components were required, retaining 99.9909% of the variance. The PCA coefficients were then linearly interpolated in ($T_{\rm eff}$, $\log g$, [M/H]) space, and the full model vector was reconstructed at each proposed MCMC position. This procedure interpolates the model spectra and photometry themselves rather than interpolating fitted parameters or discrete fit statistics.

The sampled parameters were $T_{\rm eff}$, $\log g$, [M/H], and $\log_{10}\alpha$, where $\alpha = (R/d)^2$. We adopted uniform priors within the LOWZ grid limits given above and a uniform prior $-26 < \log_{10}\alpha < -16$. The likelihood was Gaussian and used the same observational error floors and spectral-to-photometric weighting as the discrete model comparison. To account conservatively for residual atmosphere-model and interpolation uncertainties, an additional 3% systematic uncertainty was added in quadrature to each element of the weighted data-vector uncertainty. This floor was calculated relative to the larger of the absolute weighted datum and the median absolute value of the weighted data vector.

We sampled the posterior using `emcee` (Foreman-Mackey et al. 2013) with 80 walkers. The walkers were initialized near the preferred discrete LOWZ solution using a random seed of 42. We discarded an initial 1200-step burn-in phase and then ran each walker for 3000 production steps, thinning the resulting chains by a factor of 10. The estimated integrated autocorrelation times were approximately 45-47 steps for the four sampled parameters, so the production chains extended over more than 60 autocorrelation times.

C/O and K_{zz} were fixed rather than fitted simultaneously because the restricted F444W wavelength coverage does not provide sufficient independent leverage to robustly separate metallicity, C/O ratio, vertical mixing, surface gravity, and flux normalization. The resulting posterior is therefore interpreted as a LOWZ-based physical-scale estimate under fixed-chemistry assumptions, rather than as a complete atmospheric retrieval.

4.4. Molecular-opacity and Empirical Spectral Tests

To examine the molecular origin of the structure in the F444W spectrum, we carried out two complementary tests. First, we use representative ExoMolOP opacity profiles (Chubb et al. 2021) for CH_4, CO_2, and CO at $T = 700$ K and $P = 1$ bar as qualitative wavelength guides. Because cool-brown-dwarf molecular bands contain dense and overlapping rovibrational transitions, the opacity profiles are displayed at $R \sim 300$ to suppress individual line structure and emphasize the broad wavelength dependence of each opacity source. Each opacity curve is independently normalized, inverted, and rescaled to the Shabgard flux range for visualization only. No opacity-to-flux conversion is implied, and the observed Shabgard spectrum remains at its native NIRCam/F444W WFSS resolving power of $R \sim 1600$.

We then performed a fixed-atmosphere forward-model test using PICASO (Batalha et al. 2019) and the pressure-temperature and native chemistry profile of the best-ranked Sonora Elf Owl V2 (Mukherjee et al. 2024; Wogan et al. 2025) grid solution ($T_{\rm eff} = 700$ K, $\log g = 5.50$, [M/H] $= -0.50$, C/O=1.0, and $\log K_{zz} = 2.0$). The native composition is H_2/He dominated. For the molecular-opacity and empirical spectral comparisons only, we use the $R \sim 1600$ binned representation of the extracted spectrum, containing 289 samples over 4.05–4.85 μm. The original 816-pixel extraction remains the input to the main spectro-photometric atmosphere-model fitting described in Section 4.2. The PICASO thermal spectrum was calculated using the high-resolution $R = 15000$ opacity database, convolved to $R \sim 1600$, and sampled on the same 289-point, 4.05–4.85 μm wavelength grid as Shabgard. Only one positive multiplicative normalization was fitted; we applied no wavelength shift, continuum tilt, feature-specific masking, or local rescaling.

To test molecular attribution, the calculation was repeated after removing CH_4, CO_2, and CO opacity individually while keeping the pressure-temperature structure and the remaining chemistry fixed. We quantify the change using

$$\Delta\chi^2 = \chi^2_{\rm raw,no\ mol} - \chi^2_{\rm raw,full}, \tag{9}$$

where $\chi^2_{\rm raw}$ is the summed uncertainty-weighted squared residual. The significance of each change was calibrated with 5000 parametric-bootstrap realizations under the corresponding no-molecule model. We additionally repeated the comparison for matched resolving powers of $R = 1400$, 1600, and 1800.

As an empirical comparison independent of the atmosphere-model family, we also compare Shabgard with the published JWST spectra of the T8 dwarf 2MASS J0415−0935 (Alejandro Merchan et al. 2025) and the T6 dwarf JADES-GS-BD-11 (Hainline et al. 2026). The 2MASS J0415−0935 spectrum was obtained with JWST/NIRSpec G395H at $R \sim 2700$ (Alejandro Merchan et al. 2025; Jakobsen et al. 2022) and is degraded to the native Shabgard information scale ($R \sim 1600$). JADES-GS-BD-11 was observed with NIRSpec/PRISM (Hainline et al. 2026); for this comparison we degrade Shabgard to a representative PRISM information scale of $R \sim 100$, noting that the instrumental PRISM resolving power

is wavelength dependent (Jakobsen et al. 2022). In each comparison we fit only one positive multiplicative normalization and calculate the diagnostics on the unsmoothed, resolution-matched vectors.

5. Results

5.1. Cross-model Atmosphere Comparison

Figure 2 summarizes the final atmosphere-model comparison for Shabgard. The strongest result is the convergence of five independently constructed model families on $T_{\rm eff} = 700$ K: Sonora Elf Owl, LOWZ, SAND, Morley, and Sonora Bobcat. These grids treat chemistry, metallicity, vertical mixing, clouds, and evolutionary constraints differently, so their agreement establishes approximately 700 K as the principal cross-model temperature scale. ATMO selects a cooler $T_{\rm eff} = 450$ K solution, providing a model-family-dependent lower-temperature comparison while remaining within the cool brown-dwarf regime.

The surface gravities are moderate to high, although the exact value remains model-dependent. The displayed solutions span $\log g \sim 4.0$-5.5: Sonora Elf Owl gives $\log g = 5.50$, Sonora Bobcat gives 5.25, LOWZ and Morley give 5.00, and SAND and ATMO give 4.00. Thus, most of the highest-ranked solutions favor moderate-to-high gravity, and none requires an extremely low-gravity, inflated atmosphere. This is consistent with the interpretation of Shabgard as a field brown dwarf rather than a very young object.

The metallicity-sensitive grids favor subsolar metallicity, although the exact abundance is model-dependent. LOWZ gives a displayed best fit with [M/H]$= -1.00$, and SAND gives [M/H]$= -1.10$. Sonora Elf Owl and Sonora Bobcat also select subsolar metallicity, with [M/H]$= -0.50$ in both displayed best fits. In the Sonora grids used here, however, only three metallicity values are available, and [M/H]$= -0.50$ is the lowest value in the fitted grid. The Sonora fits should therefore be interpreted as showing a preference toward the low-metallicity edge of the available Sonora parameter space, rather than as a precise measurement of [M/H]$= -0.50$. Taken together with the lower-metallicity LOWZ and SAND solutions, this behavior supports a metal-poor interpretation, but the current F444W-only spectrum cannot fully separate metallicity from C/O ratio, surface gravity, and vertical mixing.

The Morley cloudy model gives a fit quality comparable to the cloud-free Sonora Bobcat model. This does not mean that a cloud feature is detected. Rather, it shows that a cloudy cool-dwarf atmosphere is allowed by the present data. In the Morley/Ackerman-Marley cloud framework, the sedimentation-efficiency parameter $f_{\rm sed}$ controls the vertical thickness of the cloud: smaller $f_{\rm sed}$ values correspond to less efficient settling and thicker, more vertically extended clouds, while larger $f_{\rm sed}$ values correspond to more efficient settling and relatively thinner clouds (Ackerman & Marley 2001; Morley et al. 2012). The best displayed Morley model has $f_{\rm sed} = 5$, so it should be interpreted as a cloudy but relatively settled/thinner-cloud solution within that model grid. The F444W-only spectrum does not provide enough wavelength leverage to distinguish this uniquely from cloud-free solutions.

Table 3 gives the numerical comparison of the best-fit atmosphere models. Sonora Elf Owl is the highest-ranked displayed model and combines the lowest balanced score with the highest cosine similarity. LOWZ and SAND follow closely and independently reinforce the preference for subsolar metallicity. Morley and Sonora Bobcat provide similarly strong spectral-shape agreement, showing that the present data allow both a cloudy-but-settled and a cloud-free atmosphere at approximately 700 K. ATMO provides a cooler 450 K comparison solution that extends the model-family temperature range; the convergence of the other five families at 700 K remains the central cross-model result.

5.2. LOWZ Posterior and Physical Scale

The LOWZ PCA-interpolated MCMC provides the only continuous posterior used in this analysis. The resulting posterior distributions and derived physical quantities are shown in Figure 3. In this fit, the sampled parameters are $T_{\rm eff}$, $\log g$, [M/H], and the dilution factor α, while C/O and K_{zz} are fixed to the values of the best LOWZ grid solution. This fixed-chemistry setup is used because the F444W-only spectrum does not provide enough independent wavelength leverage to separate metallicity, C/O ratio, vertical mixing, gravity, and normalization simultaneously.

To validate the interpolation, we performed leave-one-interior-slice-out cross-validation in $T_{\rm eff}$, $\log g$, and [M/H], rebuilding the PCA basis and interpolator after removing each parameter slice. Six principal components retain 99.9909% of the model variance. Across 2141 withheld LOWZ models, the F444W spectral interpolation has an rms error of $0.175\sigma_{\rm obs}$; near the inferred posterior, the median rms decreases to $0.077\sigma_{\rm obs}$, with a 95th percentile of $0.094\sigma_{\rm obs}$.

The LOWZ posterior gives

$$T_{\rm eff} = 718.6^{+10.6}_{-10.2}\ {\rm K}, \tag{10}$$

$$\log g = 5.13^{+0.09}_{-0.15}, \tag{11}$$

$$[{\rm M/H}] = -1.00^{+0.07}_{-0.08}, \tag{12}$$

$$\log_{10}\alpha = -21.76^{+0.02}_{-0.02}. \tag{13}$$

Using a radius prior of $R = 1.00 \pm 0.10 R_{\rm Jup}$ (Baraffe et al. 2003; Saumon & Marley 2008) to convert $\alpha = (R/d)^2$ gives

$$d = 176.2^{+18.4}_{-17.8}\ {\rm pc}, \tag{14}$$

$$M = 52.1^{+18.0}_{-16.3} M_{\rm Jup}, \tag{15}$$

where the mass is computed from $g = GM/R^2$.

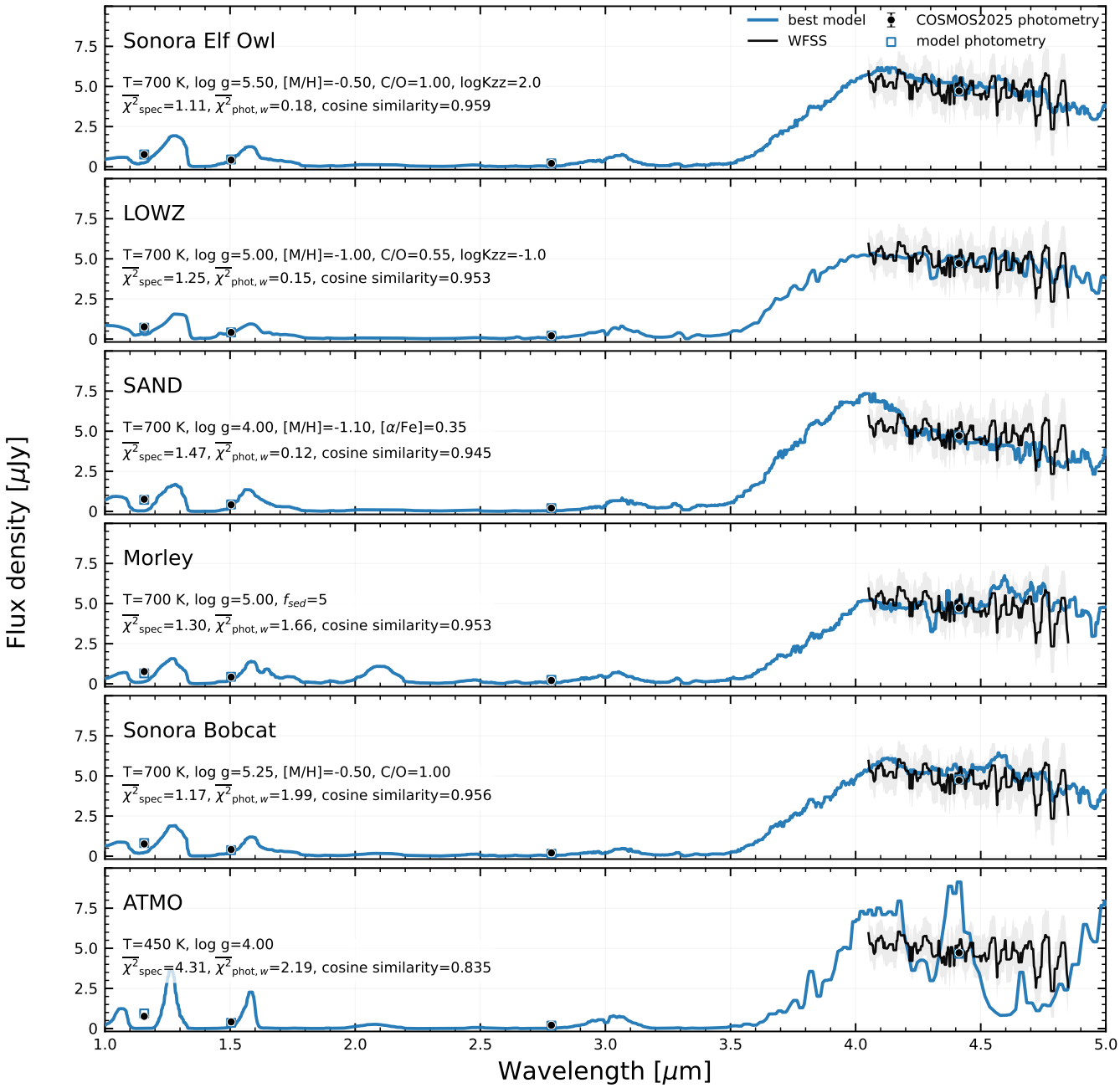


Figure 2. Best-fitting atmosphere models for Shabgard from the six model families used in the final comparison. The panels are ordered by the adopted balanced fit score, which combines the WFSS spectral agreement and the JWST/NIRCam photometric agreement. In each panel, the blue curve shows the scaled best-fitting model spectrum, the black curve shows the local-background, profile-weighted F444W WFSS spectrum, and the gray region shows the spectral uncertainty. Black points show the COSMOS2025 photometry, and open blue squares show the corresponding synthetic model photometry. The model families and references are listed in Table 2. All six model families remain within the cool brown-dwarf regime. Sonora Elf Owl, LOWZ, SAND, Sonora Bobcat, and Morley converge on $T_{\rm eff} = 700$ K, while ATMO provides a cooler $T_{\rm eff} = 450$ K solution. The Morley cloudy model provides a useful test of possible condensate-cloud opacity.

The LOWZ physical scale is higher in mass and distance than the ATMO/Sonora evolutionary checks. ATMO and Sonora Bobcat provide distances near 143–145 pc and masses near $23M_{\rm Jup}$, while LOWZ gives $d \sim 176$ pc and $M \simeq 52M_{\rm Jup}$. This difference is not surprising. LOWZ is used here as an atmosphere-only low-metallicity grid with a radius prior, whereas ATMO and Sonora Bobcat provide internally linked atmosphere/evolution solutions. The two approaches, therefore, respond differently to gravity, normalization, radius, and metallicity. Importantly, both physical scales remain substellar

Table 3
Best-fit Atmosphere-model Comparison and Physical-scale Estimates for Shabgard

Model	$T_{\rm eff}$ [K]	$\log g$	[M/H]	Other Parameters	Physical Scale/Interpretation	$\overline{\chi^2}_{\rm spec}$	$\overline{\chi^2}_{{\rm phot},w}$	Cosine
Sonora Elf Owl	700	5.50	−0.50	C/O=1.00, $\log K_{zz} = 2.0$	Best balanced score; cloud-free disequilibrium-chemistry solution.	1.11	0.18	0.959
LOWZ grid	700	5.00	−1.00	C/O=0.55, $\log K_{zz} = -1.0$	Low-metallicity grid solution; used as the basis for the MCMC posterior below.	1.25	0.15	0.953
SAND	700	4.00	−1.10	$[\alpha/{\rm Fe}] = 0.35$	Independent metal-poor solution; strongest photometric agreement among the displayed models.	1.47	0.12	0.945
Morley cloudy	700	5.00	⋯	$f_{\rm sed} = 5$	Cloudy but relatively settled/thinner-cloud solution; cloud opacity allowed but not uniquely detected.	1.30	1.66	0.953
Sonora Bobcat	700	5.25	−0.50	C/O=1.00	Cloud-free atmosphere comparison; a separate evolutionary-scale check is given in Appendix A.2.	1.17	1.99	0.956
ATMO	450	4.00	⋯	Displayed grid fit	Cooler atmosphere-grid solution; a separate evolutionary-scale check is given in Appendix A.2.	4.31	2.19	0.835
LOWZ MCMC	$718.6^{+10.6}_{-10.2}$	$5.13^{+0.09}_{-0.15}$	$-1.00^{+0.07}_{-0.08}$	$\log_{10}\alpha = -21.76^{+0.02}_{-0.02}$	With $R = 1.00 \pm 0.10 R_{\rm Jup}$: $d = 176^{+18}_{-18}$ pc and $M = 52^{+18}_{-16} M_{\rm Jup}$.	⋯	⋯	⋯

Note. The first six rows correspond to the six displayed models in Figure 2, ordered by the adopted balanced fit score.

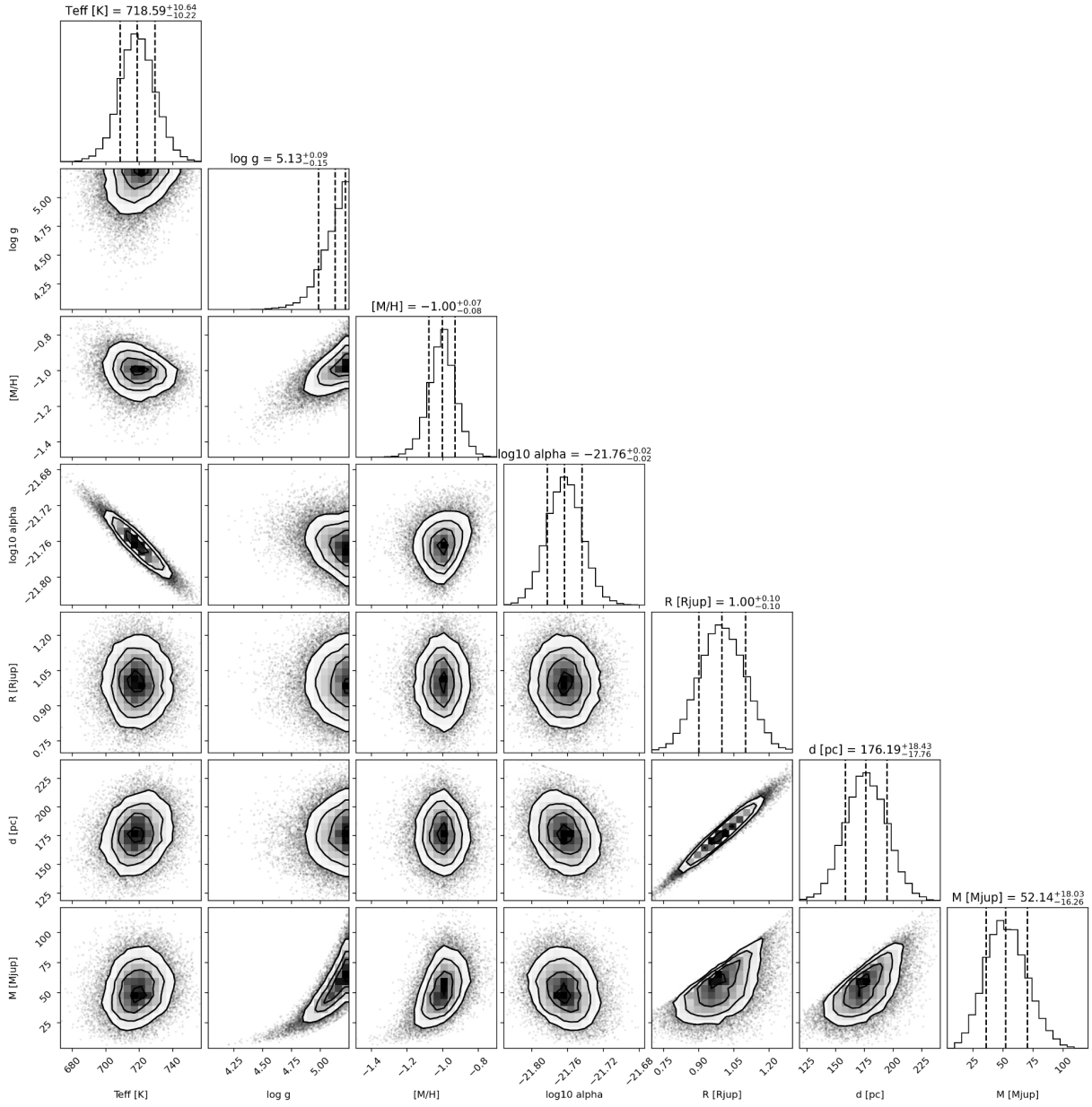


Figure 3. LOWZ PCA-interpolated posterior for Shabgard, including derived physical parameters. The sampled atmosphere parameters are $T_{\rm eff}$, $\log g$, [M/H], and $\log_{10}\alpha$, where $\alpha = (R/d)^2$. The radius is not fitted directly by the LOWZ atmosphere grid; it is drawn from an external $R = 1.00 \pm 0.10 R_{\rm Jup}$ prior. The distance follows from the dilution factor $\alpha = (R/d)^2$, and the mass follows from $g = GM/R^2$. These physical values are therefore conditional on both the LOWZ atmosphere solution and the adopted radius prior.

and place Shabgard as a foreground Galactic object along the COSMOS line of sight.

5.3. Multi-epoch Proper Motion and Tangential Velocity of Shabgard

The availability of multi-epoch JWST/NIRCam imaging provides an astrometric test of whether Shabgard is a foreground Galactic source. We measured its position in PRIMER (Donnan et al. 2024), COSMOS-Web (Casey et al. 2023; Franco et al. 2026), and COSMOS-3D (Meyer et al. 2026) imaging obtained between 2023 and 2025. The primary measurements use the same pair of observing epochs, PRIMER and COSMOS-3D, but are obtained independently from the F115W, F200W, and F356W images. The exposure midpoints recorded in the original image headers give

baselines of approximately 1.927 yr for these comparisons. We also use the F115W COSMOS-Web-COSMOS-3D measurement as a secondary astrometric check.

For each image, the source centroid was measured in a locally background-subtracted cutout using a two-dimensional Gaussian estimator. Small residual offsets between epochs were corrected using nearby compact reference sources. For each pair of images, we calculated the median displacement of the reference-source population and subtracted this local-frame offset from the displacement measured for Shabgard. Following the usual astrometric convention, the proper-motion components are

$$\mu_{\alpha^*} = \frac{\Delta\alpha^*_{\rm corr}}{\Delta t}, \qquad \mu_\delta = \frac{\Delta\delta_{\rm corr}}{\Delta t}, \tag{16}$$

where $\Delta\alpha^* = \Delta\alpha\cos\delta$ and Δt is the elapsed time between the observations (Lindegren et al. 2012; Butkevich & Lindegren 2014).

5.3.1. Annual-parallax Correction

The apparent displacement between two epochs can contain contributions from both the intrinsic proper motion and annual parallax. We therefore calculated the parallax contribution using the exposure midpoint and the barycentric JWST coordinates recorded in the `MJD-AVG`, `JWST_X`, `JWST_Y`, and `JWST_Z` keywords of the original `i2d` products. Astrometric motion relative to the Solar-system barycentre can be written in terms of the parallax factors in the local right-ascension and declination directions (Lindegren et al. 2012; Butkevich & Lindegren 2014). For two epochs, the differential parallax displacement is

$$\Delta\alpha^*_\varpi = \varpi\big(P_{\alpha^*,2} - P_{\alpha^*,1}\big), \qquad \Delta\delta_\varpi = \varpi(P_{\delta,2} - P_{\delta,1}), \tag{17}$$

where P_{α^*} and P_δ are the dimensionless parallax factors and

$$\varpi\ [\mathrm{mas}] = \frac{1000}{d\ [\mathrm{pc}]}. \tag{18}$$

The two parallax terms in Equation 17 were subtracted from the locally registered displacement before calculating the proper motion.

At a representative distance of 160 pc, the predicted differential parallax displacement for the primary PRIMER-COSMOS-3D epoch pair is only 0.62 mas. Over the model-dependent distance range of approximately 143–176 pc, the correction remains between about 0.57 and 0.70 mas. Its contribution to the inferred proper motion is therefore only about 0.32 mas yr^{-1}, and the change in the total proper-motion amplitude is approximately 0.1%.

The COSMOS-Web and COSMOS-3D observations sample more widely separated parallax phases. Their predicted differential parallax displacement is approximately 10.1 mas at 160 pc and is consequently more sensitive to the adopted distance. We therefore use this shorter-baseline measurement only as a consistency check and do not include it in the primary combined proper motion.

5.3.2. Proper-motion Measurement

The three primary measurements show consistent motion toward decreasing right ascension and declination, as illustrated in Figure 4. Evaluating the small parallax correction at the representative distance of 160 pc, the F115W comparison gives

$$(\mu_{\alpha^*},\ \mu_\delta) = (-70.36,\ -53.89)\ \mathrm{mas\ yr^{-1}}, \tag{19}$$

corresponding to

$$|\mu|_{\rm F115W} = 88.62 \pm 0.60\ \mathrm{mas\ yr^{-1}}. \tag{20}$$

For F200W, we obtain

$$(\mu_{\alpha^*},\ \mu_\delta) = (-69.76,\ -55.09)\ \mathrm{mas\ yr^{-1}}, \tag{21}$$

with

$$|\mu|_{\rm F200W} = 88.89 \pm 0.70\ \mathrm{mas\ yr^{-1}}. \tag{22}$$

The F356W comparison gives

$$(\mu_{\alpha^*},\ \mu_\delta) = (-73.05,\ -54.03)\ \mathrm{mas\ yr^{-1}}, \tag{23}$$

and

$$|\mu|_{\rm F356W} = 90.86 \pm 0.90\ \mathrm{mas\ yr^{-1}}. \tag{24}$$

Combining the three PRIMER-COSMOS-3D measurements gives

$$|\mu| = 89.17^{+0.40}_{-0.40}\ \mathrm{mas\ yr^{-1}}. \tag{25}$$

The distance dependence of the parallax correction is very small for this epoch pair. Repeating the calculation with the ATMO, Sonora Bobcat, and LOWZ distance distributions changes the median combined proper motion by less than 0.02 mas yr^{-1}.

We assessed the significance of the displacement through artificial-source injection and recovery. For each epoch pair, 500 sources constructed from an empirical representation of the target point-spread function were inserted at clean positions with approximately the same brightness as Shabgard. Two tests were performed: one in which the artificial sources were displaced by the measured motion and another in which they remained stationary. The scatter in the recovered proper motions of the moving artificial sources is approximately 0.6–0.9mas yr^{-1} for the three primary comparisons.

After scaling the recovery distributions to the header-derived time intervals, the 95th percentiles of the apparent motions of stationary sources are approximately 3.2, 5.0, and 27.1mas yr^{-1} in F115W, F200W, and F356W, respectively. The measured amplitudes exceed these limits by factors of approximately 28, 18, and 3.4. The F115W and F200W measurements therefore provide particularly strong evidence

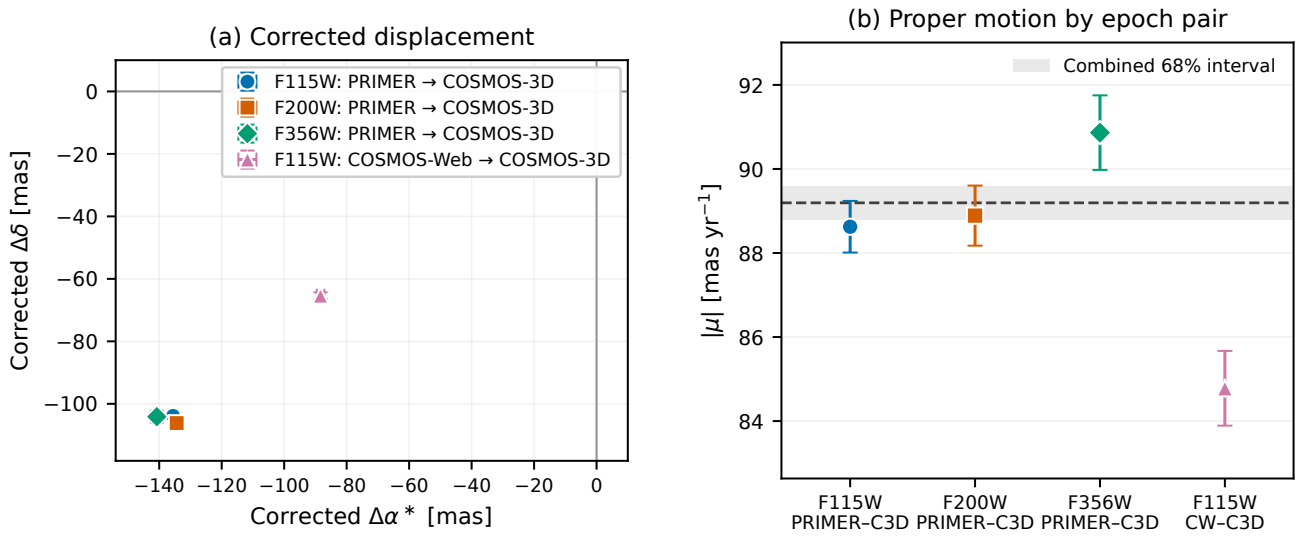


Figure 4. Multi-epoch astrometric measurements for COSMOS2025 Shabgard after local-frame registration and annual-parallax correction. Panel (a) shows the displacement components for the three same-filter PRIMER-COSMOS-3D comparisons and the additional F115W COSMOS-Web-COSMOS-3D comparison. Horizontal and vertical error bars show the robust 1σ-equivalent scatter obtained from the recovery of injected artificial sources. Panel (b) shows the corresponding total proper-motion amplitudes. The dashed horizontal line and shaded region indicate the median and central 68% interval of the combined result from the three PRIMER-COSMOS-3D measurements. The COSMOS-Web-COSMOS-3D measurement is shown as an independent check and is not included in the combined value.

that the displacement is not produced by centroid noise or local image structure. The F356W test is less constraining because its stationary-source distribution is broader, although its direction and amplitude remain consistent with the other two filters.

Because the three measurements share the same survey epochs and parts of the same local astrometric reference frame, the uncertainty in Equation 25 should be interpreted as an internal injection-recovery uncertainty. Correlated registration errors could introduce an additional contribution that is not fully represented by the formal combined interval.

5.3.3. Tangential Velocity and Galactic Context

The measured proper motion was converted to a heliocentric tangential velocity using

$$V_{\rm tan} = 4.74047\ \mu\ d, \tag{26}$$

where μ is in arcsec yr^{-1}, d is in pc, and $V_{\rm tan}$ is in km s^{-1}. This conversion is the standard relation between angular motion, distance, and transverse velocity (Johnson & Soderblom 1987; Chen et al. 2025).

We propagated the distance and astrometric uncertainties using 2×10^5 Monte Carlo realizations. In each realization, we first drew a distance from the relevant model distribution and converted it to a parallax. The corresponding parallax displacement was then calculated separately in right ascension and declination and subtracted from each measured epoch-pair displacement. The three corrected proper-motion measurements were combined, and Equation 26 was evaluated using the same distance draw. This procedure retains the weak covariance between distance, annual parallax, proper motion, and tangential velocity.

The representative ATMO and Sonora Bobcat distances of 143 and 145 pc give

$$V_{\rm tan,ATMO} \simeq 60.5\ {\rm km\ s^{-1}} \tag{27}$$

and

$$V_{\rm tan,Sonora} \simeq 61.3\ {\rm km\ s^{-1}}, \tag{28}$$

respectively.

For the LOWZ distance posterior, $d = 176.2^{+18.4}_{-17.8}$ pc, the self-consistent calculation gives

$$V_{\rm tan,LOWZ} = 74.5^{+7.7}_{-7.5}\ {\rm km\ s^{-1}}. \tag{29}$$

The model-dependent median range is therefore approximately

$$V_{\rm tan} \simeq 60\text{-}74\ {\rm km\ s^{-1}}. \tag{30}$$

Recalculating the parallax correction for every distance realization changes the median tangential velocity by less than 0.01 km s^{-1} relative to a calculation using a fixed 160-pc correction. The uncertainty in $V_{\rm tan}$ is therefore controlled mainly by the model-dependent distance rather than by annual parallax.

For comparison, the volume-limited ultracool-dwarf sample of Schmidt et al. (2007) has a mean tangential velocity of 31.5 km s^{-1} and a dispersion of 20.7 km s^{-1}. The velocity inferred for Shabgard is therefore elevated relative to the mean local ultracool-dwarf population. It is also substantially higher than the 12–17 km s^{-1} transverse velocities that Chen et al.

(2025) associated with three low-velocity thin-disk brown dwarfs in COSMOS-Web. In contrast, a distant galaxy would have an effectively negligible measurable proper motion over the approximately 1.93 yr observational baseline, so the large and consistent motion measured for Shabgard strongly disfavors a distant extragalactic interpretation.

On the other hand, Shabgard remains below the $V_{\rm tan} > 100$ km s^{-1} high-velocity population identified by Faherty et al. (2009), whose kinematics were interpreted as being associated with older thick-disk or halo ultracool dwarfs. The present result is therefore most naturally described as consistent with an older Galactic-disk object and possibly compatible with thick-disk membership. This interpretation is also qualitatively consistent with the subsolar-metallicity atmosphere solutions, but the tangential velocity alone does not provide a unique population classification.

A radial-velocity measurement is needed to calculate the full heliocentric (U, V, W) space motion and to perform a quantitative thin-disk, thick-disk, or halo membership test (Johnson & Soderblom 1987; Faherty et al. 2009). The significant motion detected independently in three NIRCam filters nevertheless strongly disfavors a stationary extragalactic interpretation and provides separate support for identifying Shabgard as a foreground Galactic ultracool dwarf.

5.4. Supplementary Random-forest Regression Cross-check

As a supplementary check on the LOWZ-based atmospheric inference, we trained regression models using the fixed-chemistry LOWZ atmosphere grid (Meisner et al. 2021), accessed with `ucdmcmc` v1.4.4 (Burgasser 2026). The input vector comprised 54 F444W-normalized spectral bins spanning 4.06–4.84 μm (effective $R \sim 307$) and three flux ratios sharing F444W as the reference band: F115W/F444W, F150W/F444W, and F277W/F444W. The spectral information was compressed using principal component analysis (PCA; Jolliffe & Cadima 2016), and random-forest regressors (Breiman 2001) were implemented using `scikit-learn` (Pedregosa et al. 2011). Spectral preprocessing, PCA, and regression were refitted within each validation fold, and each fold withheld all grid models having the target-parameter value under evaluation.

For effective temperature, 15 interior held-out slices yielded $R^2 = 0.997$, an RMSE of 15.7 K, and an MAE of 12.5 K. Combining the measurement-noise Monte Carlo realizations with the empirical held-out-slice residuals gave

$$T_{\rm eff} = 712^{+19}_{-21} \quad \text{K}. \tag{31}$$

The corresponding interval overlaps the LOWZ MCMC estimate of $718.6^{+10.6}_{-10.2}$ K. In a separate feature-set ablation, the validation RMSE decreased from 33.9 K using photometry alone and 35.4 K using the spectrum alone to 16.8 K when both were combined, indicating that the two data components provide complementary temperature information.

For metallicity, nine interior held-out slices gave $R^2 = 0.988$, an RMSE of 0.097 dex, and an MAE of 0.065 dex. The resulting estimate was

$$[\text{M/H}] = -1.50^{+0.25}_{-0.35}. \tag{32}$$

This interval does not overlap the LOWZ MCMC result of $[\text{M/H}] = -1.00^{+0.07}_{-0.08}$. Nevertheless, both independently favor a subsolar atmosphere. It is not a statistically independent measurement because it uses the same observations, F444W normalization, fixed-chemistry assumptions (C/O = 0.55 and $\log K_{zz} = -1.0$), and LOWZ model grid as the MCMC analysis. The exact metallicity should therefore be regarded as method- and model-dependent.

5.5. Molecular-opacity and Empirical Spectral Comparisons

The fixed-atmosphere PICASO calculation provides a close reconstruction of the observed F444W spectral shape. The full Sonora Elf Owl V2/PICASO atmosphere gives $\chi^2_{\rm spec} = 1.130$ and a cosine similarity of 0.957. These values are close to, but not identical to, those of the precomputed Sonora Elf Owl grid spectrum in Table 3 because the same atmospheric structure and chemistry are recomputed here through the PICASO radiative-transfer and opacity framework for the molecule-removal experiment.

Figure 5 shows the molecular-opacity comparison. The broad ExoMolOP curves in panel (a) are shown only as qualitative wavelength guides. In the physical leave-one-species-out calculation shown in panel (b), removing CH_4 opacity substantially worsens the fit, with $\Delta\chi^2 = 96.68$ and an empirical bootstrap probability $p = 2.0 \times 10^{-4}$. The result is insensitive to a reasonable change in the adopted resolving power: $\Delta\chi^2 = 97.94$, 96.68, and 95.60 for $R = 1400$, 1600, and 1800, respectively. In contrast, removing CO_2 produces only $\Delta\chi^2 = 0.048$ ($p = 0.051$), which we regard as inconclusive, while removing CO gives $\Delta\chi^2 = -5.09$ ($p = 0.959$) and is not supported by this fixed-atmosphere test.

We therefore find strong fixed-atmosphere support for CH_4 opacity contributing to the observed 4–5 μm spectral shape. We do not interpret this result as a formal CH_4 abundance measurement because the atmospheric parameters are held fixed and the available wavelength interval contains broad, overlapping molecular bands.

The empirical JWST comparison is shown in Figure 6. At the native Shabgard information scale, the T8 dwarf 2MASS J0415−0935 provides a close detailed match, with $\chi^2_{\rm spec} = 1.52$ and cosine similarity =0.939. For JADES-GS-BD-11, the comparison is performed after degrading Shabgard to the nominal PRISM resolution; the cosine similarity remains high (0.918), but the substantially larger

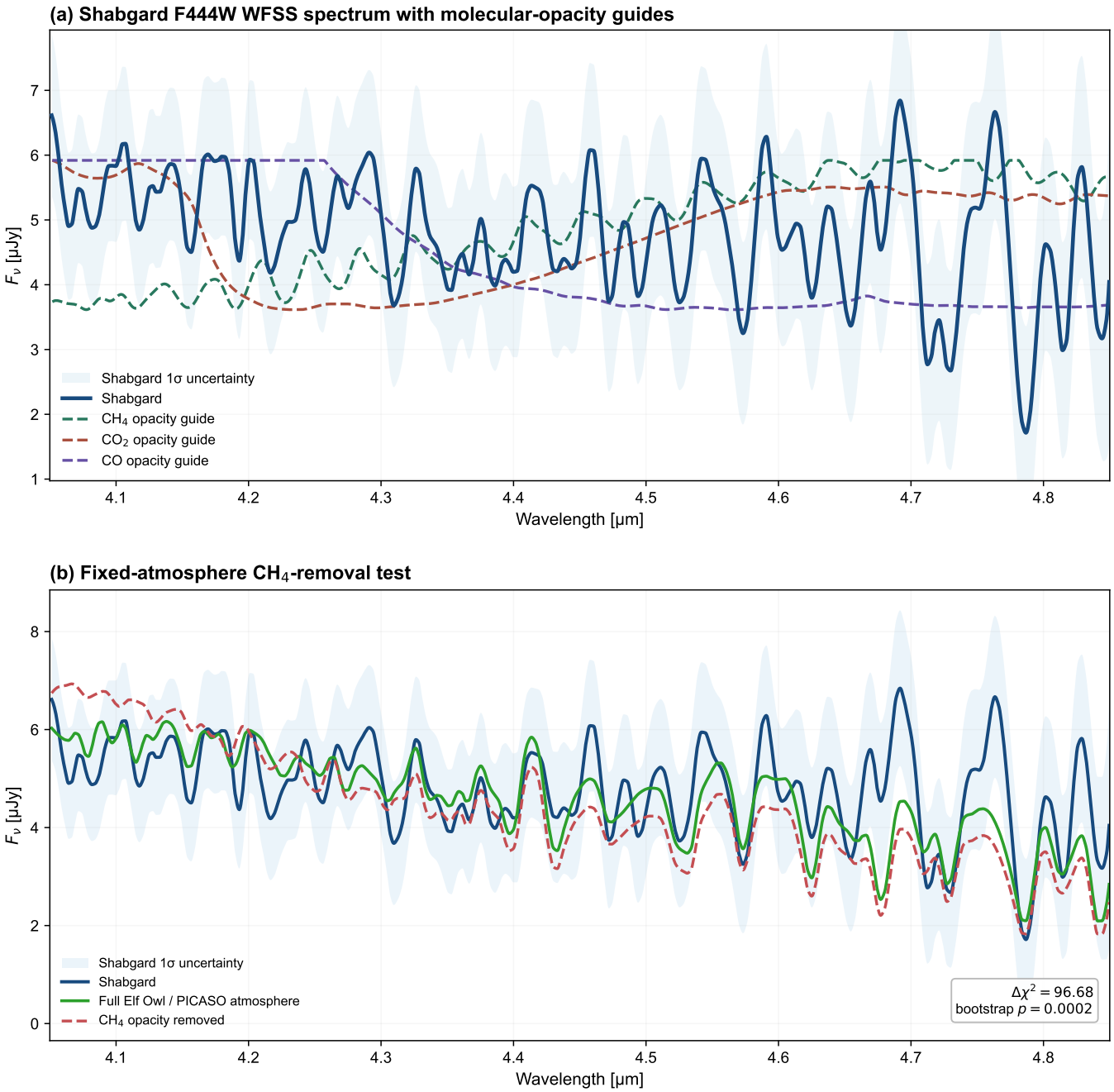


Figure 5. Molecular identification in the Shabgard F444W spectrum. (a) Shabgard is shown at its native NIRCam/WFSS resolving power ($R \sim 1600$) together with representative ExoMolOP CH_4, CO_2, and CO opacity profiles displayed at $R \sim 300$ as qualitative wavelength guides. The opacity curves are independently normalized, inverted, and rescaled and are not physical flux components. (b) Fixed-atmosphere CH_4-removal test based on the selected Sonora Elf Owl V2 atmosphere recomputed with PICASO. The green curve shows the full atmosphere and the red dashed curve shows the same fixed atmosphere with CH_4 opacity removed. Removing CH_4 worsens the fit by $\Delta\chi^2 = 96.68$, with an empirical bootstrap probability $p = 2.0 \times 10^{-4}$.

$\chi^2_{\rm spec} = 39.70$ indicates poorer wavelength-by-wavelength agreement.

Because these two comparisons contain different numbers of independent resolution elements, we do not use their absolute $\chi^2_{\rm spec}$ values as a formal subtype-selection statistic. Instead, the comparison provides an empirical spectral-shape check. The closer agreement with 2MASS J0415−0935 supports a late-T-like interpretation of Shabgard, consistent with the approximately 700 K temperature inferred from the atmosphere models, while the restricted F444W interval remains insufficient for a formal empirical spectral classification.

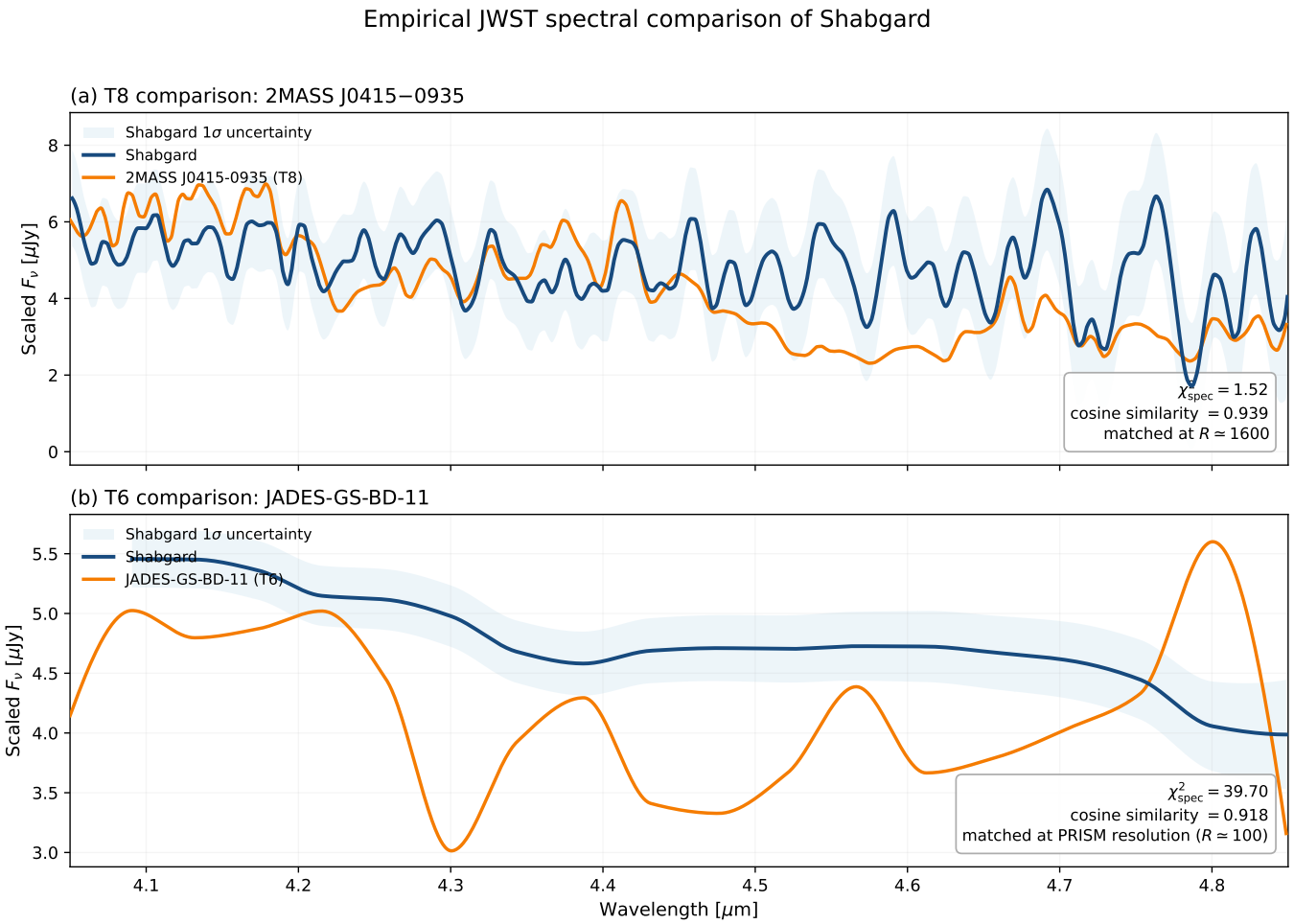


Figure 6. Direct empirical JWST spectral comparison of Shabgard with two brown dwarfs having similar effective temperatures. In panel (a), the higher-resolution 2MASS J0415−0935 NIRSpec/G395H spectrum is matched to the native Shabgard NIRCam/WFSS resolving power ($R \sim 1600$). In panel (b), Shabgard is degraded to the nominal NIRSpec/PRISM resolving power ($R \sim 100$) for comparison with JADES-GS-BD-11. A single multiplicative normalization is fitted in each comparison. The reported $\chi^2_{\rm spec}$ values use the same mean uncertainty-weighted squared-residual statistic defined in Section 4, while the cosine similarity is the same raw, uncentered diagnostic used in the atmosphere-model comparison. The plotted curves are smoothed only for visualization after the diagnostics are calculated.

6. Discussion

6.1. Why the Brown-dwarf Interpretation is Favored

Shabgard is favored as a brown-dwarf because several independent tests point in the same direction. The source was selected as a compact, red, point-source-like object from the COSMOS2025/COSMOS-Web photometric candidate catalog. It is also one of the few candidates with a centered and relatively clean COSMOS-3D F444W WFSS trace. The local-background, profile-weighted extraction gives a synthetic F444W flux consistent with the COSMOS2025 catalog photometry, so the spectrum and photometry can be compared on a common flux scale.

The atmosphere-model comparison provides the strongest physical support for the brown-dwarf interpretation. Five independent model families converge on $T_{\rm eff} = 700$ K, while ATMO provides a cooler 450 K comparison solution; the LOWZ continuous posterior independently centers near 719 K. The best-ranked solutions favor moderate-to-high gravities. This temperature scale is broadly associated with the late-T to Y-dwarf regime (Burgasser et al. 2006; Cushing et al. 2011; Filippazzo et al. 2015), although the restricted F444W wavelength coverage does not permit a formal empirical spectral classification. These solutions are not consistent with a hot stellar photosphere, and the compact morphology and stellar-template preference from the photometric selection disfavor an ordinary galaxy interpretation. A deeper JWST/NIRSpec PRISM spectrum would provide the broader wavelength coverage and higher signal-to-noise ratio required to assign a more secure empirical spectral type and to test the molecular absorption pattern expected for a late-T/Y dwarf. Complementary MIRI/LRS spectroscopy would extend this analysis into the mid-infrared, where strong molecular

features, particularly from NH_3, could provide additional constraints on the atmospheric chemistry and effective temperature (Beiler et al. 2023). The multi-epoch astrometry provides an additional test that is independent of the atmosphere fitting. The measured displacement is reproduced in three NIRCam filters and is substantially larger than the apparent motions recovered for stationary artificial sources. This proper motion strongly disfavors a stationary high-redshift source. It does not by itself establish a brown-dwarf classification, because other Galactic point sources may also have measurable motions, but its combination with the compact morphology, very red photometry, and cool atmosphere-model solutions considerably strengthens the foreground ultracool-dwarf interpretation.

6.2. Where the Model Families Agree and Where they Differ

The model families agree on three main points. First, Shabgard is cool: five grids converge at $T_{\rm eff} = 700$ K, ATMO remains in the cool regime at 450 K, and the LOWZ continuous posterior centers near 719 K. Second, the best-ranked solutions generally favor moderate-to-high gravity, although the exact value remains model-dependent. Third, the inferred physical scale is substellar, even though the exact mass differs among model assumptions.

The main differences involve metallicity, chemistry, clouds, and the mapping from atmosphere parameters to mass and distance. The metallicity-sensitive models favor subsolar abundance: LOWZ gives [M/H]$= -1.00$ in both the displayed grid fit and the MCMC posterior, and SAND gives [M/H] $= -1.10$ in the displayed comparison. Sonora Elf Owl and Sonora Bobcat also select the lowest metallicity available in the fitted Sonora grids, [M/H]$= -0.50$. This agreement at the low-metallicity edge is encouraging, but it should not be over-interpreted as a precise abundance constraint. In the F444W grism range, metallicity, C/O ratio, gravity, and vertical mixing can all affect the continuum shape and molecular opacity (Mukherjee et al. 2024). The current data are therefore better suited to identifying a cool, likely metal-poor atmosphere than to measuring a unique chemical composition.

The cloud comparison is also model-dependent. The Morley grid includes sulfide and salt condensate clouds, while Sonora Bobcat and ATMO are used here as cloud-free or effectively cloud-free comparison models. The Morley best fit has $f_{\rm sed} = 5$, which corresponds to efficient sedimentation and a relatively thin or settled cloud layer in the Ackerman-Marley framework (Ackerman & Marley 2001; Morley et al. 2012). Its best fit shows that cloud opacity is allowed, but it does not prove that clouds are present. With only the F444W window, the safest conclusion is that the data are consistent with either a cloud-free atmosphere or a cloudy atmosphere with relatively settled condensate opacity.

The physical-scale disagreement is also understandable. The ATMO and Sonora Bobcat evolutionary checks give masses near $23 M_{\rm Jup}$ and distances near 145 pc. The LOWZ atmosphere-only posterior, combined with a radius prior, gives a higher conditional mass of $52^{+18}_{-16} M_{\rm Jup}$ and a distance of 176^{+18}_{-18} pc. These values differ because the LOWZ calculation fits a dilution factor for an atmosphere grid and then imposes an external radius prior, while the ATMO/Sonora checks use evolutionary tracks that link radius, mass, gravity, temperature, and age self-consistently. The difference should therefore be treated as a systematic uncertainty in the physical scale rather than as a contradiction.

6.3. Information Content of the F444W Spectrum

The F444W grism range samples part of the 4–5 μm region in which cool brown-dwarf spectra are shaped by molecular opacity from species including CH_4, H_2O, CO, CO_2, NH_3, PH_3, H_2S, and collision-induced H_2 absorption (Tennyson & Yurchenko 2012; Phillips et al. 2020; Marley et al. 2021; Mukherjee et al. 2024). This wavelength interval therefore provides useful atmospheric information even though it is substantially narrower than a full NIRSpec spectrum.

The qualitative ExoMolOP comparison and the fixed-atmosphere PICASO experiment provide complementary information. The opacity guides show where broad molecular absorption is expected, whereas the leave-one-species-out calculation tests whether a particular opacity source is needed to reproduce the observed spectral shape. Within the selected Sonora Elf Owl V2 atmosphere, removing CH_4 produces a substantial degradation in the fit ($\Delta\chi^2 = 96.68$, bootstrap $p = 2.0 \times 10^{-4}$), and this result remains stable over $R = 1400$–1800. We therefore find strong fixed-atmosphere support for CH_4 opacity in the observed F444W spectrum. The corresponding tests do not provide comparable evidence for CO_2 or CO.

This result should nevertheless not be interpreted as a molecule-by-molecule abundance retrieval or as the identification of isolated CH_4 transitions. The molecular bands in this wavelength interval are broad and overlapping, and the PICASO experiment holds the pressure–temperature profile and remaining chemistry fixed. Broader wavelength coverage is required to marginalize simultaneously over temperature, gravity, metallicity, C/O ratio, vertical mixing, clouds, and molecular abundances.

The empirical comparison provides an independent check on the overall spectral shape. Shabgard shows substantially closer detailed agreement with the T8 dwarf 2MASS J0415 −0935 than with the T6 JADES-GS-BD-11 spectrum after the appropriate pairwise resolution matching. This supports a late-T-like interpretation, but the limited F444W wavelength range remains insufficient for a formal empirical spectral subtype.

A deeper JWST/NIRSpec spectrum would extend the comparison to multiple H_2O and CH_4 bands and provide the wavelength leverage needed for a more complete atmospheric retrieval. Complementary MIRI spectroscopy would further constrain the cool-atmosphere chemistry, particularly through NH_3 and other mid-infrared molecular features.

6.4. Distance, Kinematics, and Follow-up

The present distance estimates are ∼145–176 pc, depending on whether the physical scale is inferred from ATMO/Sonora evolutionary checks or from the LOWZ dilution factor with a radius prior. At these distances, Shabgard would be a foreground Galactic ultracool dwarf in the COSMOS field. The inferred mass is more model-dependent: ATMO/Sonora evolutionary checks favor $\sim 23 M_{\rm Jup}$, while LOWZ plus a $1 R_{\rm Jup}$ radius prior gives $\sim 52 M_{\rm Jup}$. Both values are below the hydrogen-burning limit and remain within the brown-dwarf regime.

The most useful follow-up would be broader JWST/NIRSpec or combined NIRCam+MIRI spectroscopy. A wider wavelength baseline would test the H_2O and CH_4 bands outside the F444W window, improve the measurement of the 4–5 μm molecular structure, and help separate metallicity, C/O ratio, surface gravity, vertical mixing, and cloud opacity. Such data would also allow a more secure empirical late-T/Y spectral classification.

7. Conclusions

We have presented a spectrophotometric analysis of Shabgard (COSMOS2025 ID 639188), a cool brown-dwarf identified in JWST/COSMOS-3D F444W WFSS data. The main conclusions are:

1. The atmosphere-model comparison strongly favors a cool brown-dwarf atmosphere. Sonora Elf Owl, LOWZ, SAND, Morley, and Sonora Bobcat all select $T_{\rm eff} = 700$ K, while ATMO provides a cooler $T_{\rm eff} = 450$ K comparison solution. The convergence of five independent grids at 700 K, together with the LOWZ continuous posterior at $718.6^{+10.6}_{-10.2}$ K, makes approximately 700 K the principal atmospheric temperature scale of the analysis.
2. The displayed grid solutions span $\log g = 4.0$-5.5, with most of the highest-ranked fits favoring moderate-to-high gravity. None requires an extremely low-gravity, inflated atmosphere. This is consistent with Shabgard being a field brown dwarf rather than a very young object.
3. The metallicity-sensitive grids favor subsolar metallicity. LOWZ gives [M/H] = −1.00 in the displayed grid fit and $[{\rm M/H}] = -1.00^{+0.07}_{-0.08}$ in the PCA-interpolated MCMC posterior, while SAND gives [M/H] = −1.10 in the displayed comparison. We treat this as evidence for a likely metal-poor atmosphere, but not as a final abundance measurement because the F444W-only spectrum leaves metallicity, C/O ratio, gravity, and vertical mixing partially degenerate.
4. The Morley cloudy model gives a competitive fit with $f_{\rm sed} = 5$. This corresponds to a cloudy but relatively settled/thinner-cloud solution within the Ackerman-Marley/Morley framework. Cloud opacity is therefore not ruled out, but the present data do not provide a direct cloud detection.
5. The physical scale remains model-dependent but substellar. ATMO/Sonora evolutionary checks give distances near 143–145 pc and masses near $23 M_{\rm Jup}$, while the LOWZ dilution factor combined with a $1.00 \pm 0.10 R_{\rm Jup}$ radius prior gives $d = 176^{+18}_{-18}$ pc and $M = 52^{+18}_{-16} M_{\rm Jup}$.
6. Multi-epoch NIRCam astrometry gives consistent proper-motion amplitudes of 88.6-90.9mas yr^{-1} in F115W, F200W, and F356W, with a combined value of $|\mu| = 89.17 \pm 0.40$mas yr^{-1}. Artificial-source tests show that the displacement is substantially larger than the apparent motions recovered for stationary sources. Shabgard is therefore securely identified as a Galactic source rather than a stationary extragalactic object.
7. Combining the proper motion with the model-dependent distances gives a heliocentric tangential velocity of approximately 60–74 km s^{-1}. This is elevated relative to the mean local ultracool-dwarf population and is consistent with an older Galactic-disk object, although a radial-velocity measurement is needed to calculate the full (U, V, W) motion and test thin-disk, thick-disk, or halo membership quantitatively.
8. A PCA-random-forest regression on the fixed-chemistry LOWZ grid provides an independent-method cross-check of the atmospheric inference. It yields $T_{\rm eff} = 712^{+19}_{-21}$ K, with an interval overlapping the LOWZ MCMC result, and independently supports a subsolar atmosphere with $[{\rm M/H}] = -1.50^{+0.25}_{-0.35}$. Because the regression and MCMC metallicity intervals do not overlap, the precise metallicity remains method- and model-dependent.
9. A fixed-atmosphere Sonora Elf Owl V2/PICASO test provides strong support for CH_4 opacity in the F444W spectrum: removing CH_4 worsens the fit by $\Delta\chi^2 = 96.68$, with an empirical bootstrap probability $p = 2.0 \times 10^{-4}$. Comparable support is not obtained for CO_2 or CO. An independent empirical comparison shows that Shabgard has closer detailed spectral-shape agreement with the T8 dwarf 2MASS J0415−0935 than with the T6 JADES-GS-BD-11 spectrum, supporting a late-T-like interpretation without assigning a formal spectral subtype.

Taken together, the compact morphology, red photometry, cool atmosphere-model solutions, and significant proper motion identify Shabgard as a strong foreground cool brown-dwarf, likely with a late-T/Y-like atmosphere and subsolar metallicity. Higher-signal-to-noise and broader-wavelength spectroscopy, particularly with JWST/NIRSpec and potentially MIRI, is required to assign an empirical spectral type, identify individual molecular features, and better constrain its metallicity, chemistry, and cloud properties.

Acknowledgments

We thank the referee for the constructive feedback that improved the paper. This research is based on observations made with the NASA/ESA/CSA James Webb Space Telescope. The data were obtained from the Mikulski Archive for Space Telescopes (MAST) at the Space Telescope Science Institute, which is operated by the Association of Universities for Research in Astronomy, Inc. (AURA), under NASA contract NAS 5-03127. This work uses JWST/NIRCam imaging from the COSMOS-Web program (GO-1727) and JWST/NIRCam wide-field slitless spectroscopy from the COSMOS-3D program (GO-5893; PI: K. Kakiichi). We thank the COSMOS-Web and COSMOS-3D teams for producing and making available the data products that made this analysis possible.

We thank the COSMOS-3D team for their work on the NIRCam/WFSS reduction products and for helpful clarification on the extraction and flux-calibration treatment. We also thank the brown-dwarf model and software communities whose public grids and tools made the atmosphere-model comparison possible, including SAND, Sonora, Morley, ATMO, LOWZ, and `ucdmcmc`. This work also uses JWST/NIRCam imaging from the Public Release IMaging for Extragalactic Research program (PRIMER; GO-1837; PI: J. Dunlop).

T.G. acknowledges the support of the National Science and Technology Council of Taiwan through grants 114-2112-M-007-026, 113-2112-M-007-006, and 113-2927-I-007-501. T.H. acknowledges the support of the National Science and Technology Council of Taiwan through grants 110-2112-M-005-013-MY3 and 110-2112-M-007-034. RAM acknowledges support from the Swiss National Science Foundation (SNSF) through project grant 200020_207349.

We also thank our collaborators and colleagues for valuable discussions and feedback that improved this work.

Software: Astropy (v7.2.0; Astropy et al. 2022), Astroquery (v0.4.11), NumPy (v2.4.6; Harris et al. 2020), SciPy (v1.17.1; Virtanen et al. 2020), pandas (v3.0.3), Matplotlib (v3.10.9; Hunter 2007), Photutils (v3.0.0), reproject (v0.19.0), h5py (v3.15.1), xarray (v2026.4.0), netCDF4 (v1.7.4), scikit-learn (v1.9.0; Pedregosa et al. 2011), PICASO (v4.0.1; Batalha et al. 2019), emcee (v3.1.6; Foreman-Mackey et al. 2013), corner (v2.2.3; Foreman-Mackey 2016), `ucdmcmc` (v1.4.4), the `unfold_jwst` reduction framework, and the JWST Calibration Pipeline (v1.20.2).

Data Availability

The JWST observations used in this work are publicly available through the Mikulski Archive for Space Telescopes (MAST). The analysis uses COSMOS-Web imaging (GO-1727), COSMOS-3D spectroscopy (GO-5893), and PRIMER imaging (GO-1837). The COSMOS2025 catalog is publicly available through the COSMOS2025 data release. Derived products supporting this study are available from the corresponding author upon reasonable request.

Appendix
Additional Diagnostic and Physical-scale Checks

A.1. Extraction Diagnostics for the Other Centered-trace Candidates

As described in Section 3, the one-dimensional spectrum of Shabgard was obtained through a custom local-background, profile-weighted extraction from the COSMOS-3D `unfold_jwst` two-dimensional product. Before selecting Shabgard for the detailed atmosphere-model analysis, we inspected the available two-dimensional and one-dimensional products for all photometrically selected candidates with COSMOS-3D coverage. Six objects had traces that were sufficiently centered and isolated to permit an attempted local-background extraction.

Figure A1 shows the extraction diagnostics for the remaining five centered-trace candidates. The same general procedure used for Shabgard was applied to these objects: the source trace was identified in the two-dimensional coadd, local background regions were defined on both sides of the trace, and a profile-weighted one-dimensional spectrum was extracted after background subtraction.

These five candidates were not carried forward to the detailed atmosphere-model comparison because their extracted spectra were less suitable for quantitative fitting. Depending on the object, the main limitations included a weaker continuum signal, residual structure from neighboring dispersed sources, sensitivity to the adopted background regions, or poorer agreement between the extracted F444W flux scale and the independent COSMOS2025 photometry. The selection of Shabgard was therefore based on the stability and quality of the spectral extraction before consideration of the atmosphere-model fit results. The spectra shown here are retained as extraction and candidate-selection diagnostics and should not be interpreted as ruling out a brown-dwarf nature for the other candidates.

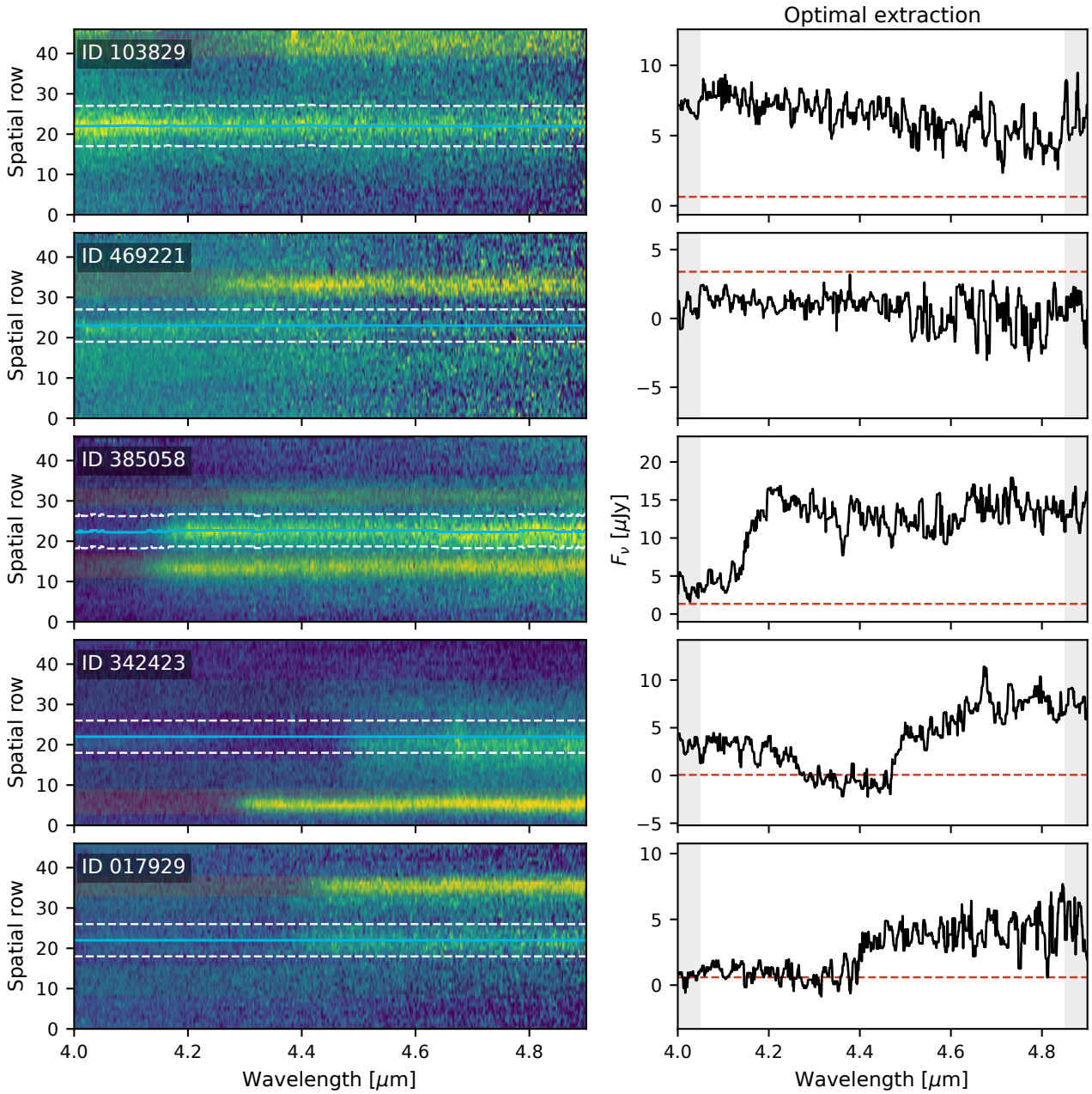


Figure A1. Local-background extraction diagnostics for the other five centered-trace candidates. For each object, the left panel shows the two-dimensional COSMOS-3D F444W WFSS spectrum, with the traced source position and adopted extraction regions marked, while the right panel shows the resulting local-background-subtracted, profile-weighted one-dimensional spectrum. These objects were not included in the detailed atmosphere-model comparison because their extractions were less stable than that of Shabgard owing to lower continuum signal, residual spectral overlap, background sensitivity, or weaker agreement with the independent F444W photometry. The main physical analysis in this paper therefore focuses on Shabgard.

A.2. Evolutionary Physical-scale Checks

The conversion of an atmosphere-model normalization into physical properties depends on the adopted relation among effective temperature, surface gravity, radius, mass, and age. We therefore performed supplementary physical-scale checks using the ATMO 2020 and Sonora Bobcat evolutionary calculations (Phillips et al. 2020; Marley et al. 2021). These checks provide an independent, model-dependent comparison with the LOWZ dilution-factor analysis presented in Section 5.2.

For each evolutionary framework, posterior samples were constructed over an age range of 0.5–13.8 Gyr. The atmosphere solution was linked to the corresponding evolutionary-model mass, radius, effective temperature, and surface

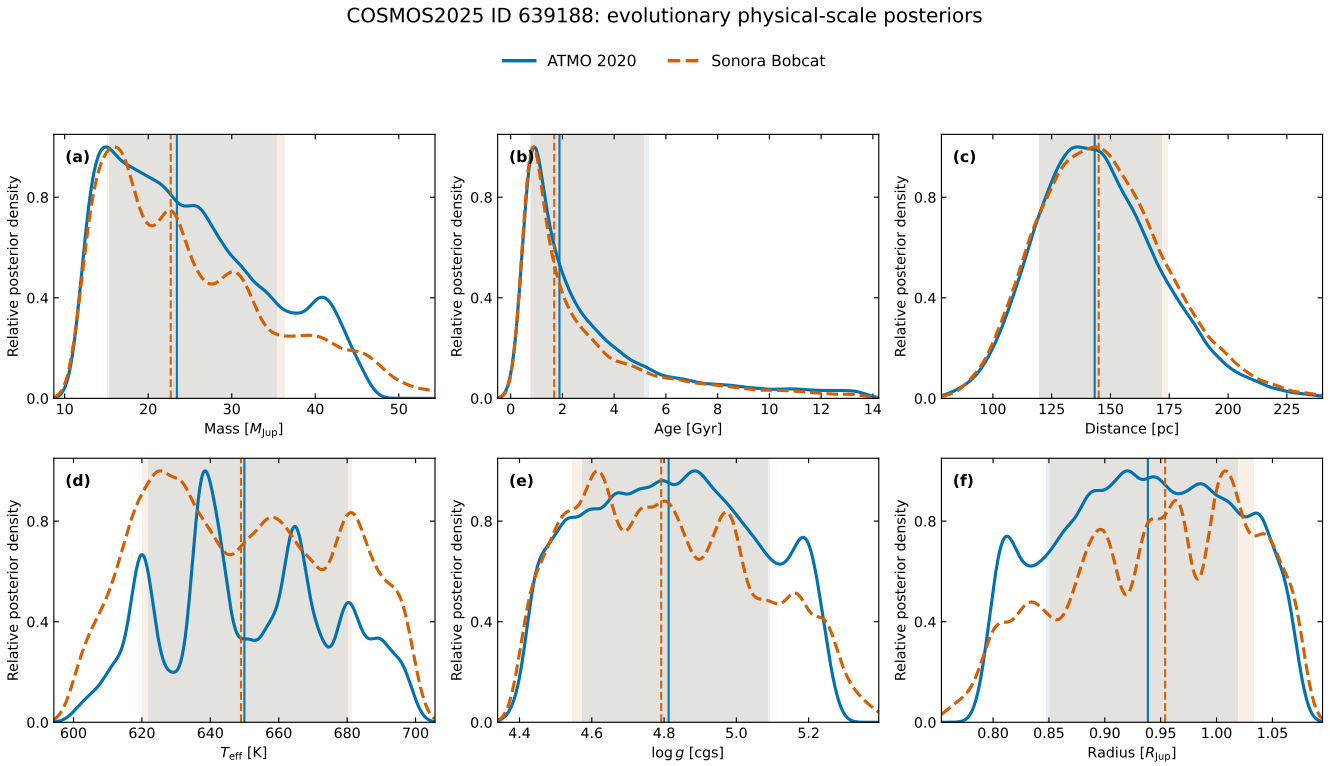


Figure A2. Marginal posterior distributions of the evolutionary physical properties of Shabgard obtained using the ATMO 2020 and Sonora Bobcat model families. The panels show (a) mass, (b) age, (c) distance, (d) effective temperature, (e) surface gravity, and (f) radius. Solid blue curves represent ATMO 2020, while dashed orange curves represent Sonora Bobcat. The vertical lines mark the posterior medians, and the shaded regions indicate the corresponding 16th-84th percentile intervals. Each distribution is independently normalized to its maximum for visual comparison. Both evolutionary frameworks favor a mass near 23 $M_{\rm Jup}$, a distance near 145 pc, an effective temperature near 650 K, a surface gravity near $\log g = 4.8$, and a radius close to one Jupiter radius. The multimodal structure visible in some derived parameters reflects the discrete and nonlinear mapping through the evolutionary-model grids.

gravity. The model normalization was then converted into a distance using the flux-dilution relation

$$\alpha = \left(\frac{R}{d}\right)^2, \tag{A1}$$

where R is the evolutionary-model radius and d is the distance. Figure A2 shows the resulting marginal posterior distributions.

The ATMO 2020 calculation gives a mass of $23.4^{+12.0}_{-8.1}\ M_{\rm Jup}$, a distance of 143^{+28}_{-24} pc, and a radius of $0.94^{+0.08}_{-0.09}\ R_{\rm Jup}$. The corresponding Sonora Bobcat values are $22.7^{+13.6}_{-7.6}\ M_{\rm Jup}$, 145^{+29}_{-25} pc, and $0.95^{+0.08}_{-0.10}\ R_{\rm Jup}$. The two frameworks also give consistent effective temperatures and surface gravities, with median values near 650 K and $\log g \simeq 4.8$, respectively.

The close agreement between the two evolutionary calculations indicates that the inferred physical scale is not strongly dependent on the choice between these model families. Nevertheless, the posteriors remain conditional on the atmosphere fits, evolutionary tracks, adopted age range, and flux normalization. They should therefore be interpreted as model-dependent consistency checks rather than direct measurements of the mass, radius, age, or distance. Together with the LOWZ dilution-factor estimate, these results support the interpretation of Shabgard as a foreground substellar object at a distance of order 150 pc.

ORCID iDs

Bahareh S. Salmasi https://orcid.org/0009-0003-0031-0527
Priyanka Jalan https://orcid.org/0000-0002-0524-5328
Tomotsugu Goto https://orcid.org/0000-0002-6821-8669
Tetsuya Hashimoto https://orcid.org/0000-0001-7228-1428
Feige Wang https://orcid.org/0000-0002-7633-431X
Tayyaba Zafar https://orcid.org/0000-0003-3935-7018
Koki Kakiichi https://orcid.org/0000-0001-6874-1321
Ece Kilerci https://orcid.org/0000-0002-9119-2313
Srivardini Ayyappan https://orcid.org/0009-0002-7530-0019
Romain A. Meyer https://orcid.org/0000-0001-5492-4522
Anilkumar Mailvaganam https://orcid.org/0009-0003-1221-1630
Tamal Mukherjee https://orcid.org/0009-0004-7639-869X
Xuanyi Lyu https://orcid.org/0009-0005-6537-9597
Imam Uzma Aalia https://orcid.org/0009-0005-0489-6232
Arihant Raidani https://orcid.org/0000-0001-5980-0174

Samuel Carlson https://orcid.org/0009-0005-2766-2850
Jose Luis Carrillo Martinez https://orcid.org/0009-0000-9947-9805
Andreas L. Faisst https://orcid.org/0000-0002-9382-9832
Marko Shuntov https://orcid.org/0000-0002-7087-0701
Hollis B. Akins https://orcid.org/0000-0003-3596-8794
Zihao Li https://orcid.org/0000-0001-5951-459X

References

Ackerman, A. S., & Marley, M. S. 2001, ApJ, 556, 872
Alejandro Merchan, S., Faherty, J. K., Suárez, G., et al. 2025, ApJ, 989, 80
Alvarado, E., Gerasimov, R., Burgasser, A. J., et al. 2024, RNAAS, 8, 134
Arnouts, S., Cristiani, S., Moscardini, L., et al. 1999, MNRAS, 310, 540
Astropy, C., Price-Whelan, A. M., Lim, P. L., et al. 2022, ApJ, 935, 167
Baraffe, I., Chabrier, G., Barman, T. S., Allard, F., & Hauschildt, P. H. 2003, A&A, 402, 701
Batalha, N. E., Marley, M. S., Lewis, N. K., & Fortney, J. J. 2019, ApJ, 878, 70
Beiler, S. A., Cushing, M. C., Kirkpatrick, J. D., et al. 2023, ApJL, 951, L48
Bezanson, R., Labbé, I., Whitaker, K. E., et al. 2024, ApJ, 974, 92
Bowler, B. P. 2016, PASP, 128, 102001
Brammer, G. B., van Dokkum, P. G., Franx, M., et al. 2012, ApJS, 200, 13
Breiman, L. 2001, MachL, 45, 5
Burgasser, A. 2026, aburgasser/ucdmcmc: v1.4.4, Zenodo, doi:10.5281/zenodo.19411337
Burgasser, A. J., Bezanson, R., Labbé, I., et al. 2024, ApJ, 962, 177
Burgasser, A. J., Geballe, T. R., Leggett, S. K., Kirkpatrick, J. D., & Golimowski, D. A. 2006, ApJ, 637, 1067
Burrows, A., Hubbard, W. B., Lunine, J. I., & Liebert, J. 2001, RvMP, 73, 719
Butkevich, A. G., & Lindegren, L. 2014, A&A, 570, A62
Casey, C. M., Kartaltepe, J. S., Drakos, N. E., et al. 2023, ApJ, 954, 31
Chabrier, G., & Baraffe, I. 2000, ARA&A, 38, 337
Chen, A. Y. A., Goto, T., Wu, C. K.-W., et al. 2025, PASA, 42, e042
Chubb, K. L., Rocchetto, M., Yurchenko, S. N., et al. 2021, A&A, 646, A21
Cushing, M. C., Kirkpatrick, J. D., Gelino, C. R., et al. 2011, ApJ, 743, 50
Donnan, C. T., McLure, R. J., Dunlop, J. S., et al. 2024, MNRAS, 533, 3222
Faherty, J. K., Burgasser, A. J., Cruz, K. L., et al. 2009, AJ, 137, 1
Faherty, J. K., Riedel, A. R., Cruz, K. L., et al. 2016, ApJS, 225, 10
Festin, F. T. A., Goto, T., Chen, A. Y.-A., Hashimoto, T., & Wu, C. K.-W. 2026, PASP, 138, 084402
Filippazzo, J. C., Rice, E. L., Faherty, J., et al. 2015, ApJ, 810, 158
Foreman-Mackey, D. 2016, JOSS, 1, 24
Foreman-Mackey, D., Hogg, D. W., Lang, D., & Goodman, J. 2013, PASP, 125, 306
Franco, M., Casey, C. M., Koekemoer, A. M., et al. 2026, ApJ, 999, 200
Gardner, J. P., Mather, J. C., Abbott, R., et al. 2023, PASP, 135, 068001
Greene, T. P., Kelly, D. M., Stansberry, J., et al. 2017, JATIS, 3, 035001
Hainline, K. N., Beiler, S. A., Burgasser, A. J., et al. 2026, arXiv:2608.14786
Hainline, K. N., Helton, J. M., Johnson, B. D., et al. 2024, ApJ, 964, 66
Harris, C. R., Millman, K. J., van der Walt, S. J., et al. 2020, Natur, 585, 357
Horne, K. 1986, PASP, 98, 609
Hunter, J. D. 2007, CSE, 9, 90
Ilbert, O., Arnouts, S., McCracken, H. J., et al. 2006, A&A, 457, 841
Jakobsen, P., Ferruit, P., Alves de Oliveira, C., et al. 2022, A&A, 661, A80
Johnson, D. R. H., & Soderblom, D. R. 1987, AJ, 93, 864
Jolliffe, I. T., & Cadima, J. 2016, RSPTA, 374, 20150202
Jurić, M., Ivezić, Ž., Brooks, A., et al. 2008, ApJ, 673, 864
Karalidi, T., Marley, M., Fortney, J. J., et al. 2021, ApJ, 923, 269
Kirkpatrick, J. D. 2005, ARA&A, 43, 195
Kirkpatrick, J. D., Gelino, C. R., Faherty, J. K., et al. 2021, ApJS, 253, 7
Kümmel, M., Walsh, J. R., Pirzkal, N., Kuntschner, H., & Pasquali, A. 2009, PASP, 121, 59
Leggett, S. K., Tremblin, P., Phillips, M. W., et al. 2021, ApJ, 918, 11
Lindegren, L., Lammers, U., Hobbs, D., et al. 2012, A&A, 538, A78
Lueber, A., & Burgasser, A. J. 2025, ApJ, 988, 31
Luhman, K. L. 2012, ARA&A, 50, 65
Marley, M. S., & Robinson, T. D. 2015, ARA&A, 53, 279
Marley, M. S., Saumon, D., Visscher, C., et al. 2021, ApJ, 920, 85
Meisner, A. M., Leggett, S. K., Logsdon, S. E., et al. 2023, AJ, 166, 57
Meisner, A. M., Schneider, A. C., Burgasser, A. J., et al. 2021, ApJ, 915, 120
Meyer, R. A., Wang, F., Kakiichi, K., et al. 2026, A&A, 712, A16
Momcheva, I. G., Brammer, G. B., van Dokkum, P. G., et al. 2016, ApJS, 225, 27
Morley, C. V., Fortney, J. J., Marley, M. S., et al. 2012, ApJ, 756, 172
Morrissey, S. J., Burgasser, A. J., de Graaff, A., McConachie, I., & Brammer, G. 2026, AJ, 171, 191
Mukherjee, S., Fortney, J. J., Morley, C. V., et al. 2024, ApJ, 963, 73
Pedregosa, F., Varoquaux, G., Gramfort, A., et al. 2011, JMLR, 12, 2825
Phillips, M. W., Tremblin, P., Baraffe, I., et al. 2020, A&A, 637, A38
Rieke, M. J., Kelly, D. M., Misselt, K., et al. 2023, PASP, 135, 028001
Rigby, J., Perrin, M., McElwain, M., et al. 2023, PASP, 135, 048001
Salton, G., Wong, A., & Yang, C.-S. 1975, Communications of the ACM, 18, 613
Saumon, D., & Marley, M. S. 2008, ApJ, 689, 1327
Schmidt, S. J., Cruz, K. L., Bongiorno, B. J., Liebert, J., & Reid, I. N. 2007, AJ, 133, 2258
Scoville, N., Aussel, H., Brusa, M., et al. 2007, ApJS, 172, 1
Shuntov, M., Akins, H. B., Paquereau, L., et al. 2025, A&A, 704, A339
Spiegel, D. S., Burrows, A., & Milsom, J. A. 2011, ApJ, 727, 57
Tennyson, J., & Yurchenko, S. N. 2012, MNRAS, 425, 21
Tu, Z., Wang, S., Chen, X., & Liu, J. 2025, ApJS, 281, 49
Virtanen, P., Gommers, R., Oliphant, T. E., et al. 2020, NatMe, 17, 261
Wang, F., Champagne, J. B., Huang, J., et al. 2026, ApJ, 1006, 39
Wang, F., Yang, J., Hennawi, J. F., et al. 2023, ApJL, 951, L4
Wang, P.-Y., Goto, T., Ho, S. C.-C., et al. 2023, MNRAS, 523, 4534
Wogan, N. F., Mang, J., Batalha, N. E., et al. 2025, RNAAS, 9, 108
Yang, J., Wang, F., Fan, X., et al. 2023, ApJL, 951, L5
Zhang, Z., Homeier, D., Pinfield, D. J., et al. 2019, MNRAS, 486, 1260